

Quantum information processing with circuit quantum electrodynamics

Alexandre Blais,^{1,2} Jay Gambetta,¹ A. Wallraff,^{1,3} D. I. Schuster,¹
S. M. Girvin,¹ M. H. Devoret,¹ and R. J. Schoelkopf¹

¹*Departments of Applied Physics and Physics, Yale University, New Haven, CT 06520*

²*Département de Physique et Regroupement Québécois sur les Matériaux de Pointe,*

Université de Sherbrooke, Sherbrooke, Québec, Canada, J1K 2R1

³*Department of Physics, ETH Zurich, CH-8093 Zürich, Switzerland*

(Dated: December 1, 2006)

We theoretically study single and two-qubit dynamics in the circuit QED architecture. We focus on the current experimental design [Wallraff *et al.*, *Nature* **431**, 162 (2004); Schuster *et al.*, cond-mat/0608693 (2006)] in which superconducting charge qubits are capacitively coupled to a single high-Q superconducting coplanar resonator. In this system, logical gates are realized by driving the resonator with microwave fields. Advantages of this architecture are that it allows for multi-qubit gates between non-nearest qubits and for the realization of gates in parallel, opening the possibility of fault-tolerant quantum computation with superconducting circuits. In this paper, we focus on one and two-qubit gates that do not require moving away from the charge-degeneracy ‘sweet spot’. This is advantageous as it helps to increase the qubit dephasing time and does not require modification of the original circuit QED. However these gates can, in some cases, be slower than those that do not use this constraint. Five types of two-qubit gates are discussed, these include gates based on virtual photons, real excitation of the resonator and a gate based on the geometric phase. We also point out the importance of selection rules when working at the charge degeneracy point.

PACS numbers: 03.67.Lx, 73.23.Hk, 74.50.+r, 32.80.-t

I. INTRODUCTION

Superconducting circuits based on Josephson junctions [1, 2] are currently the most experimentally advanced solid-state qubits. The quantum behavior of these circuits has been experimentally tested at the level of a single qubit [3, 4, 5, 6, 7] and of a pair of qubits [8, 9, 10, 11, 12]. The first quantitative experimental study of entanglement in a pair of coupled superconducting qubits was recently reported [13].

In this paper, we theoretically study quantum information processing for superconducting charge qubits in circuit QED [3, 14, 15, 16, 17, 18], focusing on two-qubit gates and under the constraints of the current experimental design. In this system qubits are coupled to a high Q transmission line resonator which acts as a quantum bus. As we will show, while this architecture is simple, it allows for many different types of qubit-qubit interactions. These gates have the advantage that they can be realized between non-nearest qubits, possibly spatially separated by several millimeters. In addition to being interesting from a fundamental point of view, this is highly advantageous in reducing the complexity of multi-qubit algorithms [19]. Moreover, it also helps in reducing the error threshold required for reaching fault-tolerant quantum computation [20]. Furthermore, some of the gates that will be presented allow for parallel operations (i.e. multiple two-qubit gates acting simultaneously on different pairs of qubits). This feature is in fact a requirement for a fault-tolerance threshold to exist [21], and this puts circuit QED on the path for scalable quantum computation.

Another aspect addressed in this paper is the ‘quality’ of realistic implementations of these gates. To quantify this quality, several measures, like the fidelity, have been proposed [22]. A fair evaluation and comparison of these measures for the different gates however requires extensive numerical calculations including realistic sources of imperfections and optimization of the gate parameters. In this work, we will rather present estimates for the quality factor [5] of the gates as obtained from analytical calculations. Initial numerical calculations have showed that, in most situations, better results than predicted by the analytical estimates can be obtained by optimization. The quality factors presented here should thus be viewed as lower bounds on what can be achieved in practice.

Five types of two-qubit gates will be presented. First, we discuss in section IV gates that are based on tuning the transition frequency of the qubits in and out of resonance with the resonator by using dc charge or flux bias. As will be discussed, this approach is advantageous because it yields the fastest gates, whose rate given by the resonator-qubit coupling frequency. A problem with this simple approach is that it takes the qubits out of their charge-degeneracy ‘sweet spot’, which can lead to a substantial increase of their dephasing rates [5]. Moreover, changing the qubit transition frequency over a wide range of frequencies can be problematic if the frequency sweep crosses environmental resonances [23].

To address these problems, we will focus in this paper on gates that do not require dc excursions away from the sweet spot. Requiring that there is no dc bias is a stringent constraint and the gates that are obtained will typically be slower. However, the resulting gate qual-

ity factor can be larger because of the important gain in dephasing time. The first of these types of gates rely on virtual excitation of the resonator (section V). This type of approach was also discussed in Refs. [14, 24] and here we will present various mechanisms to tune this type of interaction. The dispersive regime that is the basis of the schemes relying on virtual excitations of the resonator can also be used to create probabilistic entanglement due to measurement. This is discussed in section VI. Next, we consider gates that are based on real photon population of the resonator (section VII). For these gates, selection rules will set some constraints on the transitions that can be used. Finally, we discuss a gate based on the geometric phase which was first introduced in the context of ion trap quantum computation [25, 26].

Before moving to two-qubit gates, we begin in section II with a brief review of circuit QED and, in section III, with a discussion of single-qubit gates. A table summarizing the expected rates and quality factors for the different gates is presented in the concluding section.

II. CIRCUIT QED

A. Jaynes-Cummings interaction

In this section, we briefly review the circuit QED architecture first introduced in Ref. [14] and experimentally studied in Refs. [3, 15, 16, 18]. Measurement-induced dephasing was theoretically studied in Ref. [17]. As shown in Fig. 1, this system consists of a superconducting charge qubit [1, 27, 28] strongly coupled to a transmission line resonator [29]. Near its resonance frequency ω_r , the transmission line resonator can be modeled as a simple harmonic oscillator composed of the parallel combination of an inductor L and a capacitor C . Introducing the annihilation (creation) operator $a^{(\dagger)}$, the resonator can then be described by the Hamiltonian

$$H_r = \omega_r a^\dagger a, \quad (2.1)$$

with $\omega_r = 1/\sqrt{LC}$ and where we have taken $\hbar = 1$. Using this simple model, the voltage across the LC circuit (or, equivalently, on the center conductor of the resonator) can be written as $V_{LC} = V_{rms}^0(a^\dagger + a)$, where $V_{rms}^0 = \sqrt{\hbar\omega_r/2C}$ is the rms value of the voltage in the ground state. An important advantage of this architecture is the extremely small separation $b \sim 5 \mu\text{m}$ between the center conductor of the resonator and its ground planes. This leads to a large rms value of the electric field $E_{rms}^0 = V_{rms}^0/b \sim 0.2 \text{ V/m}$ for typical realizations [3, 15, 16, 18].

Multiple superconducting charge qubits can be fabricated in the space between the center conductor and the ground planes of the resonator. As shown in Fig. 1, we will consider the case of two qubits fabricated at the two ends of the resonator. These qubits are sufficiently far apart that the direct qubit-qubit capacitance is negligible. Direct capacitive coupling of qubits fabricated inside

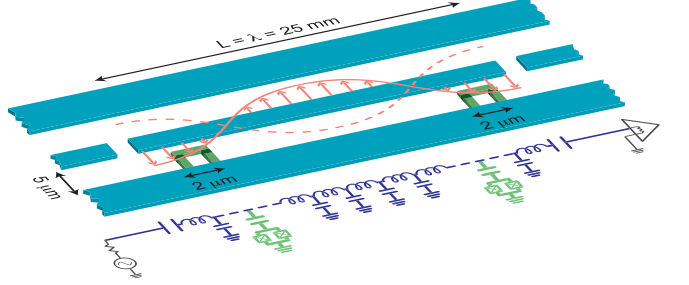


FIG. 1: (Color online) Layout and lumped element version of circuit QED. Two superconducting charge qubit (green) are fabricated inside the superconducting 1D transmission line resonator (blue).

a resonator was discussed in Ref. [24]. An advantage of placing the qubits at the ends of the resonator is the finite capacitive coupling between each qubit and the input or output port of the resonator. This can be used to independently dc-bias the qubits at their charge degeneracy point. The size of the direct capacitance must be chosen in such a way as to limit energy relaxation and dephasing due to noise at the input/output ports. Some of the noise is however still filtered by the high-Q resonator [14]. We note, that recent design advances have also raised the possibility of eliminating the need for dc bias altogether. [18]

In the two-state approximation, the Hamiltonian of the j th qubit takes the form

$$H_{qj} = -\frac{E_{elj}}{2}\sigma_{xj} - \frac{E_{Jj}}{2}\sigma_{zj}, \quad (2.2)$$

where $E_{elj} = 4E_{Cj}(1 - 2n_{gj})$ is the electrostatic energy and $E_{Jj} = E_{Jj}^{\max} \cos(\pi\Phi_j/\Phi_0)$ is the Josephson coupling energy. Here, $E_{Cj} = e^2/2C_{\Sigma j}$ is the charging energy with $C_{\Sigma j}$ the total box capacitance. $n_{gj} = C_{gj}V_{gj}/2e$ is the dimensionless gate charge with C_{gj} the gate capacitance and V_{gj} the gate voltage. E_{Jj}^{\max} is the maximum Josephson energy and Φ_j the externally applied flux with Φ_0 the flux quantum. Throughout this paper, the j subscript will be used to distinguish the different qubits and their parameters.

With both qubits fabricated close to the ends of the resonator (antinodes of the voltage), the coupling to the resonator is maximized for both qubits. This coupling is capacitive and determined by the gate voltage $V_{gj} = V_{gj}^{dc} + V_{LC}$, which contains both the dc contribution V_{gj}^{dc} (coming from a dc bias applied to the input port of the resonator) and a quantum part V_{LC} . Following Ref. [14], the Hamiltonian of the circuit of Fig. 1 in the basis of the eigenstates of H_{qj} takes the form

$$H = \omega_r a^\dagger a + \sum_{j=1,2} \frac{\omega_{aj}}{2} \sigma_{zj} - \sum_{j=1,2} g_j (\mu_j - c_j \sigma_{zj} + s_j \sigma_{xj}) (a^\dagger + a), \quad (2.3)$$

where $\omega_{a_j} = \sqrt{E_{J_j}^2 + [4E_{C_j}(1 - 2n_{g,j})]^2}$ is the transition frequency of qubit j and $g_j = e(C_{g,j}/C_{\Sigma,j})V_{\text{rms}}^0/\hbar$ is the coupling strength of the resonator to qubit j . For simplicity of notation, we have also defined $\mu_j = 1 - 2n_{g,j}$, $c_j = \cos\theta_j$ and $s_j = \sin\theta_j$, where $\theta_j = \arctan(E_{J_j}/E_{C_j}(1 - 2n_{g,j}))$ is the mixing angle [14].

When working at the charge degeneracy point $n_{g,j}^{\text{dc}} = 1/2$, where dephasing is minimized [5], and neglecting fast oscillating terms using the rotating-wave approximation (RWA), the above resonator plus qubit Hamiltonian takes the usual Jaynes-Cummings form [56]

$$H_{\text{JC}} = \omega_r a^\dagger a + \sum_{j=1,2} \frac{\omega_{a_j}}{2} \sigma_{z_j} - \sum_{j=1,2} g_j (a^\dagger \sigma_{-j} + \sigma_{+j} a). \quad (2.4)$$

This coherent coupling between a single qubit and the resonator was investigated experimentally in Ref. [3, 15, 16, 18]. In particular, in Ref. [3] high fidelity single qubit rotations were demonstrated.

B. Damping

Coupling to additional uncontrollable degrees of freedom leads to energy relaxation and dephasing in the system. In the Born-Markov approximation, this can be characterized by a photon leakage rate κ for the resonator, an energy relaxation rate $\gamma_{1,j}$ and a pure dephasing rate $\gamma_{\phi,j}$ for each qubit. In the presence of these processes, the state of the qubit plus cavity system is described by a mixed state $\rho(t)$ whose evolution follows the master equation [30]

$$\begin{aligned} \dot{\rho} = & -i[H, \rho] + \kappa \mathcal{D}[a]\rho + \sum_{j=1,2} \gamma_{1,j} \mathcal{D}[\sigma_{-j}]\rho \\ & + \sum_{j=1,2} \frac{\gamma_{\phi,j}}{2} \mathcal{D}[\sigma_{z_j}]\rho, \end{aligned} \quad (2.5)$$

where $\mathcal{D}[\hat{L}]\rho = (2L\rho L^\dagger - L^\dagger L\rho - \rho L^\dagger L)/2$ describes the effect of the baths on the system.

C. Typical system parameters

In this section, we give realistic system parameters. The resonator frequency $\omega_r/2\pi$ will be assumed to be between 5 and 10 GHz. The qubit transition frequencies can be chosen anywhere between about 5 to 15 GHz, and are tunable by applying a flux through the qubit loop. In the schematic circuit of Fig. 1, both qubits are affected by the externally applied field, but the effect on each qubit will depend on the qubit's loop area. Coupling strengths $g/2\pi$ between 5.8 and 100 MHz have been realized experimentally [15, 18] and couplings up to 200 MHz should be feasible.

Rabi frequencies of 50 MHz were obtained with a sample of moderate coupling strength $g/2\pi = 17$ MHz [3] and an improvement by at least a factor of two is realistic.

The cavity damping rate κ is chosen at fabrication time by tuning the coupling capacitance between the resonator center line and its input and output ports. Quality factors up to $Q \sim 10^6$ have been reported for under-coupled resonators [29, 31], corresponding to a low damping rate $\kappa/2\pi = \omega_r/2\pi Q \sim 5$ KHz for a $\omega_r/2\pi = 5$ GHz resonator. This results in a long photon lifetime $1/\kappa$ of 31 μ s. To allow for fast measurement, the coupled quality factor can also be reduced by two or more orders of magnitude.

Relaxation and dephasing of a qubit in this system were measured in Ref. [3]. There, $T_1 = 7.3$ μ s and $T_2 = 500$ ns were reported. These translate to $\gamma_1/2\pi = 0.02$ MHz and $\gamma_\phi/2\pi = (\gamma_2 - \gamma_1/2)/2\pi = 0.31$ MHz.

III. 1-QUBIT GATES

Single qubit gates are realized by pulses of microwaves on the input port of the resonator. Depending on the frequency, phase and amplitude of the drive, different logical operations can be realized. External driving of the resonator can be described by the Hamiltonian

$$H_{\text{D}} = \sum_k (\varepsilon_k(t) a^\dagger e^{-i\omega_{d_k} t} + \varepsilon_k^*(t) a e^{+i\omega_{d_k} t}), \quad (3.1)$$

where $\varepsilon_k(t)$ is the amplitude and ω_{d_k} the frequency of the k th external drive. Throughout this paper, the k subscript will be used to distinguish between the different drives and the drive-dependent parameters.

For simplicity of notation, we first consider the situation where there is a single qubit and drive present. We will also assume that the qubit is biased at its optimal point and use the RWA. The Hamiltonian describing this situation is $H = H_{\text{JC}} + H_{\text{D}}$ with $j = k = 1$.

Logical gates are realized with microwaves pulses that are substantially detuned from the resonator frequency. In this case, it is convenient to displace the field operators using the time-dependent unitary operator

$$D(\alpha) = \exp(\alpha a^\dagger - \alpha^* a). \quad (3.2)$$

The displaced Hamiltonian reads

$$\begin{aligned} \tilde{H} = & D^\dagger(\alpha) H D(\alpha) - i D^\dagger(\alpha) \dot{D}(\alpha) \\ = & \omega_r a^\dagger a + \frac{\omega_a}{2} \sigma_z - g (a^\dagger \sigma_- + \sigma_+ a) \\ & - g (\alpha^* \sigma_- + \alpha \sigma_+), \end{aligned} \quad (3.3)$$

where we have chosen $\alpha(t)$ to satisfy

$$\dot{\alpha} = -i\omega_r \alpha - i\varepsilon(t) e^{-i\omega_d t}. \quad (3.4)$$

In the case where the drive amplitude ε is independent of time, and by moving to a frame rotating at the frequency ω_d for both the qubit and the field operators, we get

$$\tilde{H} = \Delta_r a^\dagger a + \frac{\Delta_a}{2} \sigma_z - g (a^\dagger \sigma_- + \sigma_+ a) + \frac{\Omega_R}{2} \sigma_x, \quad (3.5)$$

where we have dropped any transient in $\alpha(t)$. In the above expression, we have defined $\Delta_r = \omega_r - \omega_d$ which is the detuning of the cavity from the drive, $\Delta_a = \omega_a - \omega_d$ the detuning of the qubit transition frequency from the drive and Ω_R is the Rabi frequency:

$$\Omega_R = 2 \frac{\varepsilon g}{\Delta_r}. \quad (3.6)$$

In the limit where Δ_r is large compared with the resonator half-width $\kappa/2$, the average photon number in the resonator can be written as $\bar{n} \approx (\varepsilon/\Delta_r)^2$. In this case, the Rabi frequency takes the simple form $\Omega_R \approx 2g\sqrt{\bar{n}}$ expected from the Jaynes-Cummings model.

We note that the effect of damping can be taken into account by performing the transformation (3.2) on the master equation (2.5) rather than on Schrödinger's equation. For completeness, this is done in appendix A. Since in this paper we are interested in the qubit dynamics under coherent control rather than measurement, we will be working in the regime where $\Delta_r > \kappa$ and as such can safely ignore the effect of κ on Ω_R . For a detailed discussion of measurement in this system, see Ref. [17].

A. On-resonance: bit-flip gate

For quantum information processing, it is more advantageous to work in the dispersive regime where $\Delta = \omega_a - \omega_r$ is much bigger than the coupling g . One advantage of this regime is that the pulses aimed at controlling the qubit are far detuned from the resonator frequency and are thus not limited in speed by its high quality factor. Another advantage is that the high quality resonator filters noise at the far detuned qubit transition frequency and effectively enhances the qubit lifetime [14].

To take into account that we are working in this dispersive regime, we eliminate the direct qubit-resonator coupling by using the transformation

$$U = \exp \left[\frac{g}{\Delta} (a^\dagger \sigma_- - a \sigma_+) \right]. \quad (3.7)$$

Using the Hausdorff expansion to second order in the small parameter $\lambda = g/\Delta$

$$e^{-\lambda X} H e^{\lambda X} = H + \lambda [H, X] + \frac{\lambda^2}{2!} [[H, X], X] + \dots \quad (3.8)$$

with $X = (a^\dagger \sigma_- - a \sigma_+)$, yields [14]

$$\begin{aligned} H_x &\approx \Delta_r a^\dagger a + \frac{1}{2} \left(\Delta_a + 2\chi \left[a^\dagger a + \frac{1}{2} \right] \right) \sigma_z + \frac{\Omega_R}{2} \sigma_x \\ &\approx \Delta_r a^\dagger a + \frac{\tilde{\Delta}_a}{2} \sigma_z + \frac{\Omega_R}{2} \sigma_x, \end{aligned} \quad (3.9)$$

where we have defined $\chi = g^2/\Delta$ and $\tilde{\Delta}_a = \tilde{\omega}_a - \omega_d$ with $\tilde{\omega}_a = \omega_a + \chi$. Since the resonator is driven far from the frequency band $\omega_r \pm \chi$ where cavity population

can be large, we have that $\langle a^\dagger a \rangle \sim 0$ (this is because we are working in a displaced frame with respect to the resonator field). As a result, we have therefore dropped the ac-Stark shift in the second line of the above expression.

By choosing $\tilde{\Delta}_a = 0$, the above Hamiltonian generates rotations around the x axis at a rate Ω_R . These Rabi oscillations have already been observed experimentally in circuit QED with close to unit visibility [3]. Changing $\tilde{\Delta}_a$, Ω_R and the phase of the drive can be used to rotate the qubit around any axis on the Bloch sphere [32].

In the situation where many qubits are fabricated in the resonator and have different transition frequencies, the qubits can be individually addressed by tuning the frequency of the drive accordingly. It should therefore be possible to individually control several qubits in the circuit QED architecture.

B. Off-resonance: phase gate

It is useful to consider the situation where the drive is sufficiently detuned from the qubit that it cannot induce transitions, but is of large enough amplitude to significantly ac-Stark shift the qubit transition frequency due to virtual transitions. To obtain an effective Hamiltonian describing this situation, we start by adiabatically eliminating the effect of direct transitions of the qubit due to the drive. This is be done by using on Eq. (3.5) the transformation

$$U = \exp [\beta^* \sigma_+ - \beta \sigma_-] \quad (3.10)$$

to second order in the small parameter $\beta = \Omega_R/2\Delta_a$. In a second step, we again take into account the fact that the qubit is only dispersively coupled to the resonator by using the transformation of Eq. (3.7) to second order. These two sequential transformation yield

$$H_z \approx \Delta_r a^\dagger a + \frac{1}{2} \left(\tilde{\Delta}_a + \frac{1}{2} \frac{\Omega_R^2}{\Delta_a} \right) \sigma_z. \quad (3.11)$$

The last term in the parenthesis is an off-resonant ac-Stark shift caused by virtual transitions of the qubit. This shift can be used to realize controlled rotation of the qubit about the z axis. The rate of this gate can be written in terms of the average photon number \bar{n} inside the resonator as $\sim 2g\sqrt{\bar{n}} \times (\Omega_R/2\Delta_a)$. To get fast rotations, one must therefore choose large values of the coupling constant g and large \bar{n} while keeping the ratio $\Omega_R/2\Delta_a$ small to prevent real transitions.

Finally, it is important to point out that in the situation where multiple qubits are present inside the resonator, each qubit will suffer a frequency shift when other qubits are driven. These frequency shifts will have to be taken into account or canceled by additional drives.

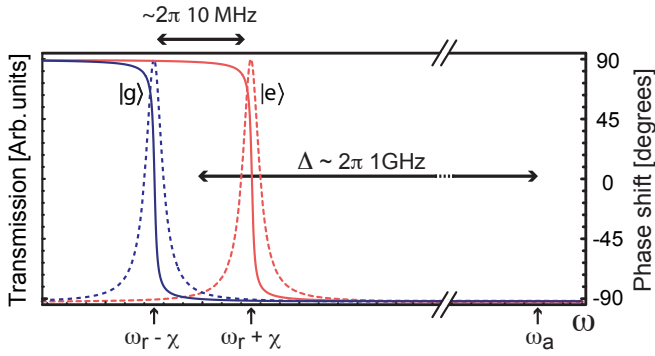


FIG. 2: (Color online) Resonator transmission (dashed lines) and corresponding phase shifts (full lines) for the two qubit states (blue: ground, red: excited). The numbers are calculated using $g/2\pi \sim 100 \text{ MHz}$ and $g/\Delta \sim 0.1$. At the far detuned frequencies required for single qubit gates, the phase shift of the resonator field does not depend on the qubit state. In this case, there is negligible entanglement between the resonator and the qubit.

C. Coherent control vs. measurement

As mentioned above, in the dispersive regime, driving the cavity close to its resonance frequency leads to a measurement of the qubits. As discussed in Refs. [14, 17], this is due to entanglement of the qubit with the resonator field generated by the term $\chi a^\dagger a \sigma_z$ of Eq. (3.9). Indeed, because of this term, the resonator frequency is pulled to $\omega_r \pm \chi$ depending on the state of the qubit. The possible resonator transmissions, corresponding to the qubit in the ground (blue) or excited (red) state, are shown (dashed lines) along with the corresponding phase shifts (full lines) in Fig. 2.

As is seen from this figure, only around $\omega_r \pm \chi$ is there significant phase shift and/or resonator transmission change for the information rate about the qubit's state to be large at the resonator output [17]. In other words, only around these frequencies is entanglement between the resonator and the qubit significant. However, when coherently controlling the qubit using the flip and phase gates discussed above, the resonator is irradiated far from $\omega_r \pm \chi$. As shown in Fig. 2, since we are working in the dispersive regime where $|\Delta| \gg g$, there is no significant phase difference in the resonator output between the two states of the qubit at these very detuned frequencies. As a result, there is no significant unwanted entanglement with the resonator when coherently controlling the qubit.

An additional benefit of working at these largely detuned irradiation frequencies is that the resonator is only virtually populated and the speed of the gates is not limited by the high Q of the resonator. These two aspects lead to high quality single qubit gates [3].

The above discussion can be made more quantitative by introducing the rate Γ_m of dephasing induced by the control drive (corresponding to measurement-induced de-

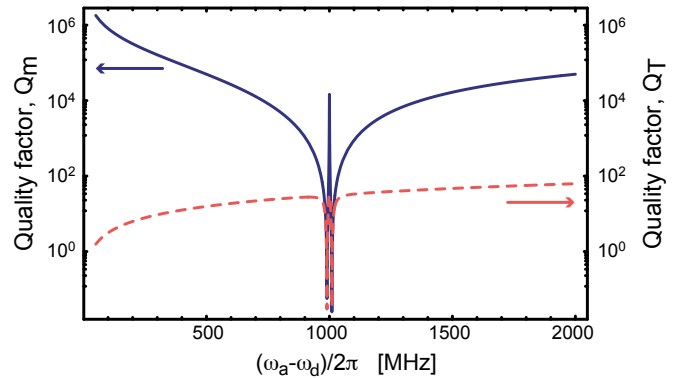


FIG. 3: (Color online) Quality factor of the phase gate, with respect to the measurement-induced dephasing rate Γ_m (blue, full line) and with respect to $\gamma_2 + \Gamma_m$ (red, dashed line) where $1/\gamma_2 = 500 \text{ ns}$. This is plotted vs. the detuning between the control drive and the qubit transition frequency. The amplitude ε of the drive is chosen such that $\Omega_R/2\Delta_a = 0.1$ for all values of the detuning. The other parameters are $g/2\pi = 100 \text{ MHz}$, $g/\Delta = 0.1$ and $\kappa/2\pi = 0.5 \text{ MHz}$. The discontinuity in Γ_m around $(\omega_a - \omega)/2\pi = \Delta = 1000 \text{ MHz}$ is due to the fact at that frequency, the drive is on resonance with the resonator and therefore corresponds to a measurement. This is not a region where a phase gate would be operated.

phasing) [17]:

$$\Gamma_m = \frac{\kappa \chi^2 (\bar{n}_+ + \bar{n}_-)}{(\kappa/2)^2 + \Delta_r^2 + \chi^2} \quad (3.12)$$

where

$$\bar{n}_\pm = \frac{\varepsilon^2}{(\kappa/2)^2 + (\Delta_r \pm \chi)^2}, \quad (3.13)$$

is the steady-state average photon number inside the resonator for a qubit in the ground (−) or excited (+) state. In practice, this rate will always be much smaller than the intrinsic dephasing rate $1/T_2$ of the qubit. For example, for the bit-flip gate, a Rabi rate of $\Omega_R/2\pi = 100 \text{ MHz}$ with $g/2\pi = 100 \text{ MHz}$ and $g/\Delta = 0.1$ yields a measurement-induced dephasing time $1/\Gamma_m$ of the order of a few milliseconds. Clearly, this is not a limitation in practice. This is illustrated for the phase gate in Fig. 3 where the quality factor

$$Q_\phi = \frac{\Omega_R^2/2\Delta_a}{2\Gamma_\phi} \quad (3.14)$$

is plotted as a function of the detuning of the drive with respect to the qubit transition frequency. In this figure, the full blue line is the quality factor (Q_m) calculated using the measurement-induced dephasing rate Γ_m and the dashed red line the quality factor (Q_T) using the total rate $\Gamma_T = \gamma_2 + \Gamma_m$ assuming a dephasing time $1/\gamma_2$ of 500 ns.

For the phase gate, a dephasing time of $1/\gamma_2 = 500 \text{ ns}$ with a rate of $\Omega_R^2/4\pi\Delta_a = 40 \text{ MHz}$ at a detuning

$(\omega_a - \omega_d)/2\pi = 2000$ MHz yields a quality factor of ~ 60 . For the bit-flip gate, a Rabi rate of 100 MHz yields a quality factor of ~ 157 .

D. AC-dither: phase gate

Another approach to produce a single-qubit phase gate, is to take advantage of the quadratic dependence of the qubit transition frequency on the gate voltage (or flux) to shift the qubit transition frequency. This can be done by modulation of these control parameters at a frequency that is adiabatic with respect to the qubit transition frequency.

Focussing on the single qubit Hamiltonian (2.2), we take $n_g(t) = n_g^{\text{dc}} + n_d(t)$, where $n_d(t) = n_g^{\text{ac}} \sin(\omega_{\text{act}} t)$ is a modulation of the gate voltage that is slow compared to the qubit transition frequency. In this situation, it is useful to move to the adiabatic basis. The relation between the original (σ_j) and adiabatic $(\tilde{\sigma}_j)$ basis Pauli operators is given by

$$\begin{aligned}\sigma_z &= \cos \Theta(t) \tilde{\sigma}_z - \sin \Theta(t) \tilde{\sigma}_x, \\ \sigma_x &= \sin \Theta(t) \tilde{\sigma}_z + \cos \Theta(t) \tilde{\sigma}_x,\end{aligned}\quad (3.15)$$

where $\Theta(t) = \arctan[E_{\text{el}}(t)/E_J]$. In this basis, the qubit Hamiltonian reads

$$\bar{H} = -\frac{\omega_a^{\text{ad}}(t)}{2} \tilde{\sigma}_z, \quad (3.16)$$

with $\omega_a^{\text{ad}}(t) = \sqrt{E_J^2 + \{4E_C[1 - 2n_g^{\text{dc}} - 2n_d(t)]\}^2}$ the instantaneous splitting. Because of the quadratic dependence with gate charge, the average part of the qubit splitting is larger than its bare value. For example, setting $n_g = 1/2$ and assuming small dither amplitude, we obtain

$$\omega_a^{\text{ad}} \approx E_J + 16 \frac{E_C^2}{E_J} (n_g^{\text{ac}})^2 \quad (3.17)$$

which should be compared to the bare value E_J . Here, we have dropped terms rotating at $2\omega_{\text{ac}}$ and higher order in the dither amplitude. Voltage ac-dither can therefore be used to blue-shift the qubit transition frequency (flux dither around the flux sweet would cause a red shift). As will be discussed below, this can also be used to couple qubits when the dither frequency is larger than the coupling strength (but still slow with respect to the qubit transition frequency).

Because ac-dither acts as a continuous spin-echo [33], it can be realized with minimal dephasing of the qubit. It therefore appears to be more advantageous than dc bias of the control parameters. For example, if the qubit is dc-biased Δn_g away from the charge degeneracy point, $n_g^{\text{dc}} = 1/2 + \Delta n_g$, noise $\delta n_g(t)$ in the bias will cause dephasing due to fluctuations $(\partial \omega_a / \partial n_g) \delta n_g(t)$ in the qubit transition frequency. As illustrated in Fig. 4, if the dc-offset Δn_g is small compared to the dither amplitude n_g^{ac} ,

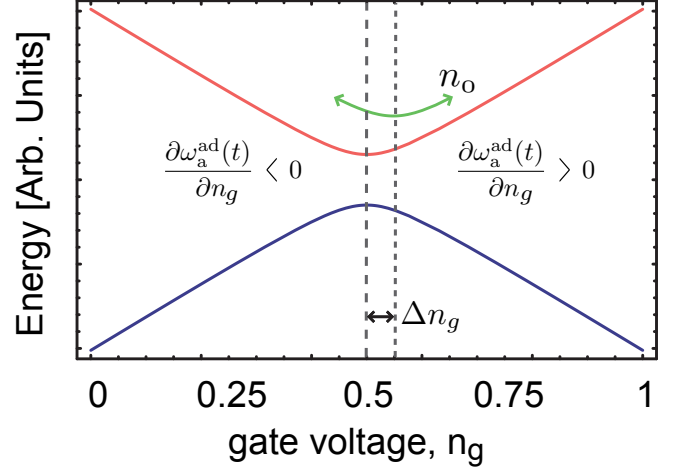


FIG. 4: (Color online) Refocussing due to ac-dither. The qubit energy splitting is shown as a function of gate charge. Ac-dither acts as refocussing by sampling the positive and negative dependence of $\omega_a^{\text{ad}}(t)$ with n_g .

then under dither, both signs of $\partial \omega_a / \partial n_g$ will be probed leading to (partial) cancelation of the unwanted fluctuating phase.

This cancelation can be seen more explicitly by assuming small excursions away from the charge degeneracy point such that $\Theta(t) \approx -\lambda(\Delta n_g + n_g^{\text{ac}} \sin \omega_{\text{act}} t)$, where we have defined $\lambda \equiv 8E_C/E_J$. Assuming that the qubit is not too deep in the charge regime such that λn_g^{ac} is small, we expand to first order in Δn_g and n_g^{ac} to obtain

$$\begin{aligned}\bar{H} \approx & -\frac{\omega_a^{\text{ad}}(t)}{2} \tilde{\sigma}_z \\ & + 4E_C \delta n_g(t) [-\lambda \Delta n_g J_0(\lambda n_g^{\text{ac}}) - 2J_1(\lambda n_g^{\text{ac}}) \sin \omega_{\text{act}} t] \tilde{\sigma}_z \\ & + 4E_C \delta n_g(t) [J_0(\lambda n_g^{\text{ac}}) - 2\lambda \Delta n_g J_1(\lambda n_g^{\text{ac}}) \sin \omega_{\text{act}} t] \tilde{\sigma}_x,\end{aligned}\quad (3.18)$$

where the $J_n(z)$ are Bessel functions of the first kind. In this expression, we have dropped higher order Bessel functions and have added the gate charge noise $\delta n_g(t)$ to $n_g(t)$.

The second term in Eq. (3.18), proportional to $\tilde{\sigma}_x$, leads to pure dephasing T_ϕ while the last term leads to mixing of the qubit. Focusing on pure dephasing, we obtain from the Golden rule

$$\begin{aligned}\frac{1}{T_\phi} \approx & \frac{1}{2} \left(\frac{64E_C^2}{E_J} \right)^2 \left\{ \Delta n_g^2 S_{\delta n_g}(0) \right. \\ & \left. + \frac{(n_g^{\text{ac}})^2}{4} [S_{\delta n_g}(-\omega_{\text{ac}}) + S_{\delta n_g}(+\omega_{\text{ac}})] \right\},\end{aligned}\quad (3.19)$$

where $S_{\delta n_g}(\omega_{\text{ac}})$ is the spectral density of the charge noise.

For both the dc and ac bias, the dephasing rate $1/T_\phi$ increases linearly with the amplitude of the shift of the transition. However, blue shifting of the qubit using ac-dither n_g^{ac} produces less dephasing than using the static

bias Δn_g provided that the dither frequency is much higher than the characteristic frequency of the noise so that

$$S_{\delta n_g}(\pm\omega_{\text{ac}}) \ll S_{\delta n_g}(0). \quad (3.20)$$

This approach should therefore efficiently protect the qubit from low frequency (i.e. $1/f$) noise. Assuming $\Delta n_g = 0$ and using Eq. (3.17), the quality factor of this gate can be estimated as $Q \sim (E_J/64E_C^2)^2/(S_{\delta n_g}(-\omega_{\text{ac}}) + S_{\delta n_g}(+\omega_{\text{ac}}))$. This type of stabilization of logical gate by ac-fields was also studied in Ref. [34].

IV. DIRECT COUPLING BY VARIABLE DETUNING

In the layout of Fig. 1, qubit-qubit interaction must be mediated by the resonator. It is therefore reasonable to expect that the limiting rate on two-qubit gates be the coupling strength g . Gates at this rate can be implemented by taking the qubits in and out of resonance with the resonator frequency. When a qubit is far off resonance, it only dispersively couples to the resonator through the coupling $\chi a^\dagger a \sigma_z$, where $\chi = g^2/\Delta$. This interaction can be made small by working at large detunings Δ . In this situation there is no significant qubit-resonator interaction. The interaction is turned on by tuning the qubit transition frequency back in resonance with the resonator. In this case, vacuum Rabi flopping at the frequency $2g$ will entangle the qubit and the resonator. It is known from ion-trap quantum computing [35, 36], and is further discussed in Section VII D, how to use this type of interaction to mediate qubit-qubit entanglement.

Tuning of the qubit transition frequency could be realized by applying flux pulses through the individual qubit loop. This would require adding flux lines in proximity to the qubits. Voltage bias using individual bias lines could also be used, but this likely introduce more noise than flux bias. Moreover, in both cases, this will take the qubits away from their sweet spot, possibly increasing their dephasing rates [5]. Alternatively, Wallquist *et al.* have suggested that a similar tuning of Δ can be realized by fabricating a resonator whose frequency is itself tunable [37]. While this is a promising idea, one drawback is that any noise in the parameter controlling the resonator frequency will lead to dephasing of photon superpositions, lowering the expected gate quality.

In addition to dc-bias, it is possible to use any of the rf approaches discussed in the previous section to tune the qubit transition frequency. Moreover, the FLICFORQ protocol [38], discussed in the next section and in appendix C could also be used. As shown in appendix C, this would yield qubit-resonator coupling at the rate $g/2$. However, for these approaches to be useful here, very large rf amplitudes would be required to cover the large

range of frequency needed to turn on and off the qubit-resonator interaction. This is especially true in the presence of many qubits fabricated in the same resonator.

In summary, this type of gate relying on tuning of the qubit or resonator frequency is advantageous because it operates at the optimal rate g . However, it requires either additional bias lines and extra dephasing or large amplitude rf-pulses. In the next sections, we will focus on gates that do not require additional tuning but only rely on rf-drive of the resonator of more moderate amplitudes. While these gates will be typically slower than the gates discussed here, they can be implemented without modification of the original circuit QED design and do not suffer from the above problems. Gates relying on direct tuning of the qubit transition frequency will be further discussed elsewhere.

V. 2-QUBIT GATES: VIRTUAL QUBIT-QUBIT INTERACTION

In this section, we expand the discussions of Ref. [14] on two-qubit gates using virtual excitations of the resonator. To minimize dephasing, we will work with both qubits at charge degeneracy ($\Delta n_g = 0$). In the rotating wave approximation, the starting point is therefore Eq. (2.4). To avoid excitation of the resonator, we assume that both qubits are strongly detuned from the resonator $|\Delta_j| = |\omega_{a_j} - \omega_r| \gg g_j$. In this situation, we adiabatically eliminate the resonant Jaynes-Cummings interaction using the transformation

$$U = \exp \left[\frac{g_1}{\Delta_1} (a^\dagger \sigma_{-1} - a \sigma_{+1}) + \frac{g_2}{\Delta_2} (a^\dagger \sigma_{-2} - a \sigma_{+2}) \right]. \quad (5.1)$$

To second order in the small parameters g_j/Δ_j , this yields [14, 39, 40, 41]

$$H_{2q} \approx \omega_r a^\dagger a + \sum_{j=1,2} \frac{\tilde{\omega}_{a_j}}{2} \sigma_{z_j} + \frac{g_1 g_2 (\Delta_1 + \Delta_2)}{2 \Delta_1 \Delta_2} (\sigma_{+1} \sigma_{-2} + \sigma_{-1} \sigma_{+2}), \quad (5.2)$$

where, as in section §III A, we have assumed that the cavity is in the vacuum state and have taken $\tilde{\omega}_{a_j} = \omega_{a_j} + \chi_j$. It is simple to generalize the above expression for an arbitrary number of qubits coupled to the same mode of the resonator. The last term in the above Hamiltonian describes swap of the qubit states through virtual interaction with the resonator. Evolution under this Hamiltonian for a time $t = \pi \Delta_1 \Delta_2 / 2g_1 g_2 (\Delta_1 + \Delta_2)$ will generate a $\sqrt{i\text{SWAP}}$ gate [14]. This gate, along with the single qubit gates discussed in section III, form a universal set for quantum computation [42].

In the situation where the qubits are strongly detuned from each other, energy conservation suppresses this flip-flop interaction. This is most easily seen by going to a frame rotating at $\tilde{\omega}_{a_j}$ for each qubit. In this frame, when

the qubits are strongly detuned, the interaction term is oscillating rapidly and averages out. In this situation, the effective qubit-qubit interaction is for all practical purposes turned off. On the other hand, for $\tilde{\omega}_{a_1} = \tilde{\omega}_{a_2}$, the interaction term does not average and the interaction is effective.

To turn on and off this virtual interaction, it is necessary to change the detuning between the qubits. There are several ways to do this in the circuit QED architecture. One possible approach is to directly change the transition frequency of the qubits using, as described in section II, using flux or voltage as control parameters. However, as can be seen from eq. (3.19), moving the gate charge away from the sweet spot will rapidly increase the dephasing rate [5, 43].

A. Off-resonant ac-Stark shift

The off-resonant ac-Stark shift discussed in section III B provides another way to tune the qubits in and out of resonance. In this situation, one must generalize the Hamiltonian of Eq. (5.2) to include off-resonant microwave fields. This is done in appendix B in the presence of three independent fields and two qubits. Two of the fields, of amplitudes ε_1 and ε_2 , are used to coherently control the state of the qubits while the third, of amplitude ε_3 is used to readout the state of the qubits.

In this section, it is sufficient to take into account a single drive ε_1 , assumed to be strongly detuned from any resonances. The resulting effective Hamiltonian [5th term of Eq. (B10)] contains the swap term already obtained in the absence of coherent drive in Eq. (5.2). The effect of the drive is to shift the qubit transition to

$$\omega''_{a_j} = \omega_{a_j} + \frac{\Omega_{R_j}^2}{2\Delta_{a_j}} + 2\frac{g_j^2}{\Delta'_j} \left(\langle a^\dagger a \rangle + \frac{1}{2} \right), \quad (5.3)$$

where $\Delta'_j = \omega_{a_j} + \Omega_{R_j}^2/2\Delta_{a_j} - \omega_r$ is the shifted detuning also entering in the renormalized swap rate.

The strategy is then to chose $\omega_{a_1} \neq \omega_{a_2}$ such that the swap gate is effectively turned off in the idle state. The interaction is turned on by choosing a drive amplitude and frequency such that $\omega''_{a_1} = \omega''_{a_2}$. This condition can be satisfied with a single drive provided that $g_1 \neq g_2$. A master equation simulation of this off-resonant ac-Stark tuning is illustrated in Fig. 5.

B. AC-Dither

In the same way as the off-resonant ac-Stark shift, ac-dither discussed in section III D can be used to effectively tune on resonance a pair of qubits (ac-dither being a low frequency version of the off-resonant ac-Stark shift). In this situation, the dither frequency must be faster than the swap rate between the qubit but still adiabatic with respect to the qubit transition frequencies. Moreover,

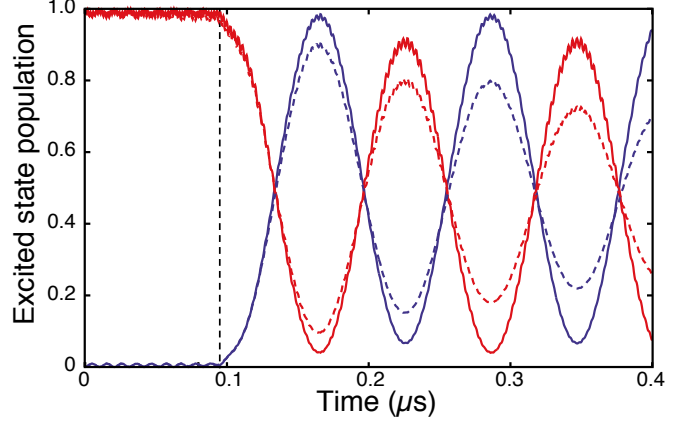


FIG. 5: (Color online) Master equation simulation of the excited state population of qubit one (blue) and qubit two (red) as a function of time. Full lines: no relaxation and dephasing. Dashed lines: finite relaxation and dephasing. The qubits are initially detuned from each other with no drive applied. A drive, bringing the shifted qubit transition frequencies in resonance, is applied at the time indicated by the vertical dashed line. At this time, the two-qubit state start to swap. The parameters are: $g_1/2\pi = 80$ MHz, $g_2/2\pi = 120$ MHz, $\omega_r/2\pi = 5$ GHz, $\omega_{a_1}/2\pi = 7.1$ GHz, $\omega_{a_2}/2\pi = 7.0$ GHz, $\omega_{d_1}/2\pi = 432.23$ MHz. For the dashed lines, cavity decay was taken as $\kappa/2\pi = 0.22$ MHz and the qubits decay rates were taken to be identical and equal to $\gamma_1/2\pi = 0.02$ MHz and $\gamma_\phi/2\pi = 0.31$ MHz.

similarly to the off-resonant ac-Stark shift, both qubits will be blue shifted by the ac-dither. The qubits can nevertheless be tuned in resonance by taking advantage of their different direct capacitance to the input or output ports (as discussed in section II A) and by using different E_C/E_J ratios.

C. FLICFORQ

Another approach to tune off-resonant qubits is to use the so-called FLICFORQ protocol (Fixed LInear Couplings between Fixed Off-Resonant Qubits) [38]. In this protocol, one is interested in tuning the effective interaction between a pair of qubits that are interacting through a fixed linear coupling. The coupling is assumed to be off-diagonal in the computational basis such that when the qubits are detuned, the coupling is only a small perturbation and can be safely neglected. The interaction is effectively turned on by irradiating each qubit at its respective transition frequency and choosing the amplitude of the drives such that one of the Rabi sidebands for one qubit is resonant with a Rabi sideband of the other qubit. In this situation, the effective coupling becomes first order in the bare coupling.

In circuit QED, FLICFORQ can be used in the dispersive regime to couple a qubit to the resonator or to couple a pair of qubits together. As shown in appendix C, the resonance condition for the first case is $\Delta = -\Omega_R$

and this leads to the effective qubit-resonator coupling $(g/2)(a^\dagger\sigma_- + a\sigma_+)$, at the charge degeneracy point and in the RWA. The interaction is first order in the coupling g , but of reduced strength.

Similarly, two qubits that are dispersively coupled to the resonator and detuned from each other can be coupled using FLICFORQ. For simplicity, we again work at the charge degeneracy point for both qubits and use the rotating approximation on the qubit-resonator couplings. To turn on the interaction, two coherent drives of frequency $\omega_{d_j} \approx \omega_{a_j}$ are used. Since the qubits are irradiated at their transition frequency, the results of appendix B cannot be used directly. The corresponding effective Hamiltonian is derived in appendix D. At one of the possible sideband matching conditions and in a quadruply rotating frame (see Appendix D), the resulting effective Hamiltonian is

$$H_{\text{FF}} \approx \omega_r a^\dagger a + \frac{g_1 g_2 (\Delta'_1 + \Delta'_2)}{16 \Delta'_1 \Delta'_2} (\sigma_{y_1} \sigma_{y_2} + \sigma_{z_1} \sigma_{z_2}), \quad (5.4)$$

where $\Delta'_j = \omega'_{a_j} - \omega_r$ with

$$\omega'_{a_{1(2)}} = \omega_{a_{1(2)}} + 2 \frac{\Omega_{R_{12(21)}}^2}{\Delta_{a_{12(21)}}}. \quad (5.5)$$

the shifted qubit frequency. In this expression, we have introduced $\Omega_{R_{jk}} = 2g_j \varepsilon_k / (\omega_r - \omega_{d_k})$ the Rabi frequency of qubit j with respect to drive k and $\Delta_{a_{jk}} = \omega_{a_j} - \omega_{d_k}$. This effective qubit-qubit coupling is sufficient, along with single qubit gates, for universal quantum computation. Moreover, as expected from Ref. [38], in the FLICFORQ protocol, the qubit-qubit coupling strength is reduced by a factor of 8 with respect to the bare coupling strength.

D. Fast entanglement at small detunings

The rates for the two-qubit gates described above are proportional to $g \times (g/\Delta)$, where g/Δ must be small for the dispersive approximation to be valid. An advantage of the dispersive regime is that the resonator is only virtually populated and therefore photon loss is not a limiting factor. The drawback is that unless g is large, dispersive gates can be slow.

It is interesting to see whether this rate can be increased by working at smaller detunings. In this situation, residual entanglement with the resonator can lead to reduced fidelities. As an example, we take for simplicity $g_1 = g_2 = g$ and $\omega_{a_1} = \omega_{a_2} = \omega_a$. Choosing

$$\Delta = \frac{2\sqrt{2}g}{\sqrt{4m^2 - 1}}, \quad (5.6)$$

where $m \geq 1$ is an integer, one can easily verify that starting from $|ge0\rangle$ or $|eg0\rangle$ at $t = 0$, the qubits are in a

maximally entangled state and the resonator in the state $|0\rangle$ after a time

$$T = \frac{\pi}{\Delta}. \quad (5.7)$$

Two-qubit entanglement can therefore be realized in a time $\sim 1/g$ and with a small detuning $\Delta \sim g$, without suffering from spurious resonator entanglement when starting from $|ge0\rangle$ or $|eg0\rangle$.

It is also simple to verify that $|gg0\rangle$ only picks up a phase factor after time T . However, starting from $|ee0\rangle$ leads to leakage to $|gg2\rangle$ at time T and therefore to unwanted entanglement with the resonator. As a result, while the simple procedure described here is not an universal 2-qubit primitive for quantum computation, it can nevertheless lead to qubit-qubit entanglement at a rate which is close to the cavity coupling rate g . We will describe in Section VII D an approach based on Ref. [36] to prevent this type of spurious resonator-qubit entanglement.

Since the cavity is populated by real rather than virtual photons during this procedure, it is important to estimate photon loss. Starting from $|ge0\rangle$ or $|eg0\rangle$, the maximum photon number in the cavity is given by $n_{\text{max}} = (4m^2 - 1)/8m^2$. The worst case scenario for the rate of photon loss is then $\Gamma = n_{\text{max}}\kappa$. The gate quality factor, considering only photon loss, is therefore $Q \sim 2\pi T^{-1}/\Gamma = 32\sqrt{2}gm^2/[\kappa(4m^2 - 1)^{3/2}]$. For $g/2\pi = 200$ MHz, $\kappa/2\pi = 1$ MHz and $m = 1$, this yields a large quality factor of $Q \sim 1700$.

E. Summary

The gates discussed in this section (apart from Sec. V D) rely on virtual population of the resonator. A disadvantage of these gates is that they will typically be slow. All of them roughly go as $g \times (g/\Delta)$ where g/Δ is a small parameter. Taking $g/\Delta \sim 0.1$ and $g/2\pi = 200$ MHz, we see that the rates of these gates will realistically not exceed 20 MHz. Although not very large, this rate nevertheless exceeds substantially the typical decay rates γ_1 , γ_ϕ and κ of circuit QED [3, 15, 16] and should be sufficiently large for the experimental realization of these ideas. An advantage of these virtual gates is however that, since the resonator field is only virtually populated, the gates do not suffer from photon loss. As a result, these gates could still be realized with a resonator of moderate Q factor (which is advantageous for fast measurement [3]).

It is also interesting to point out that, in the situation where there are more than two qubits fabricated in the resonator, the same approach can be used to entangle simultaneously two or more pairs of qubits. This is done, for example, by taking $\omega_{a_1} = \omega_{a_2} \neq \omega_{a_3} = \omega_{a_4}$ while still in the dispersive regime. It is simple to verify that this corresponds to two entangling gates acting in parallel on the two pairs of qubits. This type of classical parallelism

is an important requirement for a fault-tolerant threshold to exist [21].

Finally, we point out that the dispersive coupling can also be used to couple $n > 2$ qubits simultaneously. This is done by tuning the n qubits in resonance with each other but all still in the dispersive regime. This leads to multi-qubit entanglement in a single step.

VI. CONDITIONAL ENTANGLEMENT BY MEASUREMENT

As discussed in section III C and in more detail in Ref. [3, 14, 15, 16, 17], measurement can be realized in this system by taking advantage of the qubit-state dependent resonator frequency pull. In the presence of a single qubit, the resonator pull is $\chi\sigma_z$ and becomes $\sum_j^n \chi_j\sigma_{z_j}$ in the n -qubit case. If the pulls χ_j are different for all j 's and large enough with respect to the resonator linewidth κ , each of the different n -qubit states $\{|ggg\dots g\rangle, |egg\dots g\rangle, |gegg\dots g\rangle, \dots, |eee\dots e\rangle\}$ pulls the cavity frequency by a different amount. In this situation, it should be possible to realize single shot QND measurements of the n -qubit state. In a test of Bell inequalities, this multi-qubit readout capability would offer a powerful advantage over separate measurement of each qubit. Indeed, in the latter case the effective readout fidelity would be the product of the individual readout fidelities.

The situation is also interesting in the case where the pulls χ are equal. For example, in the two qubit case, when $\chi_1 = \chi_2 = \chi$ (and taking $\omega_{a_1} = \omega_{a_2} = \omega_a$ for simplicity), the dispersive Hamiltonian of equation (5.2) can be written as

$$H_{2q} \approx [\omega_r + \chi(\sigma_{z_1} + \sigma_{z_2})] a^\dagger a + \sum_{j=1,2} \frac{1}{2} (\omega_a + \chi) \sigma_{z_j} + \chi (\sigma_{+1}\sigma_{-2} + \sigma_{-1}\sigma_{+2}). \quad (6.1)$$

While this Hamiltonian is not QND for measurement of σ_{z_j} , it is QND for measurement of $(\sigma_{z_1} + \sigma_{z_2})$ since $[(\sigma_{z_1} + \sigma_{z_2}), H_{2q}] = 0$.

More interestingly, in this situation, the states $\{|ge\rangle, |eg\rangle\}$ while they may have different Lamb shifts have the same cavity pull. This implies that they cannot be distinguished by this measurement. The consequence of this observation can be made more explicit by rewriting (6.1) as

$$H_{2q} = \omega_r a^\dagger a + \chi (|\psi_+\rangle\langle\psi_+| - |\psi_-\rangle\langle\psi_-|) + \frac{1}{2} \left[\omega_a + 2\chi \left(a^\dagger a + \frac{1}{2} \right) \right] (|ee\rangle\langle ee| - |gg\rangle\langle gg|), \quad (6.2)$$

where $|\psi_\pm\rangle = (|ge\rangle \pm |eg\rangle)/\sqrt{2}$ are Bell states. As a result, the projection operators corresponding to measurement of the cavity pull are $\Pi_g = |gg\rangle\langle gg|$, $\Pi_e = |ee\rangle\langle ee|$

and $\Pi_{\text{Bell}} = |\psi_+\rangle\langle\psi_+| + |\psi_-\rangle\langle\psi_-|$, with $\sum_{k=g,e,\text{Bell}} \Pi_k = 1$.

An initial state $|\psi_i\rangle$ will thus, with probability $\langle\psi_i|\Pi_{\text{Bell}}|\psi_i\rangle$, collapse to a state of the form $|\psi_f\rangle = c_+|\psi_+\rangle + c_-|\psi_-\rangle$. Since the Bell states $|\psi_\pm\rangle$ are eigenstates of H_{2q} , further evolution will keep the projected state in this subspace. For certain unentangled initial states [e.g. $(|g\rangle + |e\rangle) \otimes (|g\rangle + |e\rangle)/2$, which is created by $\pi/2$ pulses on each qubit], the state after measurement will be a maximally entangled state. As a result, conditioned on the measurement of zero cavity pull, Bell states can be prepared. This type of entanglement by measurement for solid-state qubits was also discussed by Ruskov and Korotkov [44].

VII. 2-QUBIT GATES: QUBIT-QUBIT INTERACTION MEDIATED BY RESONATOR EXCITATIONS

In this section, we consider gates that actively use the resonator as a means to transfer information between the qubits and to entangle them. More precisely, we will take advantage of the so-called red and blue sideband transitions. We first start by a very brief overview of ion-trap quantum computing to show the similarities and differences with circuit QED and then present various protocols adapted to circuit QED. We discuss the realization of quantum gates based on these sideband transitions in section VII D.

A. Ion-trap quantum computation

Sideband transitions are used very successfully in ion-trap quantum computation [45, 46]. This approach to ion-trap quantum computing was first discussed by Cirac and Zoller [35] and, more recently, was adapted to two-level atoms by Childs and Chuang [36]. Following closely Ref. [36] the Hamiltonian describing a trapped ion is

$$H = \omega_r a^\dagger a + \frac{\omega_a}{2} \sigma_z - \lambda \cos[\eta(a^\dagger + a) - \omega t] \sigma_x, \quad (7.1)$$

where ω_r is the frequency of the relevant mode of oscillation of the ion in the trap, ω is the laser frequency, $\eta = \sqrt{k^2/2Nm\omega_r}$ is the Lamb-Dicke parameter and λ is the amplitude of the magnetic field produced by the driving laser [36]. Assuming $\eta \ll 1$ and choosing the laser frequency $\omega = \omega_a + n\omega_r$, the only part of the interaction term that is not rapidly oscillating and thus does not average out is

$$H_{\text{n-blue}} \approx \frac{\lambda\eta^n}{2n!} (a^{\dagger n} \sigma_+ + a^n \sigma_-). \quad (7.2)$$

For $\omega = \omega_a - n\omega_r$, we get

$$H_{\text{n-red}} \approx \frac{\lambda\eta^n}{2n!} (a^{\dagger n} \sigma_- + a^n \sigma_+). \quad (7.3)$$

These correspond to blue and red n-phonon sideband transitions, respectively. It is known that these transitions, along with single qubit gates, are universal for quantum computation on a chain of ions [36].

We first note that the rate of the sideband transitions scales with λ which itself depends on the (variable) laser amplitude. In circuit QED, we will see that the (fixed) qubit-resonator coupling g takes the role of the parameter λ . Moreover, while the Hamiltonian (7.1) allows for all orders of sideband transitions, we will see that when working at the charge degeneracy point, the symmetry of the circuit QED Hamiltonian only allows sideband transitions of even orders. Finally, it is interesting to point out that the Hamiltonian (7.1) also describes a superconducting qubit magnetically coupled to a resonator. In that situation, the qubit would be fabricated at an anti-node of current in the resonator. The zero-point fluctuations of the current generate a field that couples to the qubit loop. For example, a superconducting charge qubit magnetically coupled to the transmission line resonator would have in its Hamiltonian a term of the form $\lambda \cos[\eta(a^\dagger + a) + \bar{\theta}] \sigma_x$, where $\lambda = E_J$ and $\eta = \pi M I_{\text{rms}}^0 / \Phi_0$ with M the mutual inductance between the center line of the transmission line, I_{rms}^0 the rms value of the vacuum fluctuation current on the center line in the ground state [47, 48], Φ_0 is the superconducting flux quantum and $\bar{\theta}$ is controlled by the dc flux bias.

An important difference between trapped ions and the superconducting flux qubit analog is that in the first case λ scales with the laser amplitude while, in the second case, it is equal to the Josephson energy. The latter can only be so large in practice and is difficult to tune rapidly. Finally, we point out that solid-state qubits, in contrast to ions, have a natural spread in transition frequencies. This allows to address the qubits individually with global pulses, without requiring individual bias lines to tune them.

B. Sideband transitions in Circuit QED

Our starting point to study sideband transitions in circuit QED is the two-qubit Hamiltonian of Eq. (2.3). Here, we keep the gate charge dependence and do not initially make the rotating wave approximation. The effective Hamiltonian describing the sideband transitions in circuit QED is obtained in appendix B. As discussed above, in this appendix we consider the presence of two qubits and three coherent drives. Two of these drives, of frequency $\omega_{d1,2}$ and amplitude $\varepsilon_{1,2}$, are used to drive the sideband transitions. The third drive, of frequency ω_{d3} and amplitude ε_3 , is used to measure the state of the system. For simplicity of notation, in this section we focus on a single qubit coupled to the resonator and drop the j index.

The red and blue sideband transitions, illustrated in Fig. 6, are given by the last two lines of Eq. (B10). These correspond to single and two-photon sideband transi-

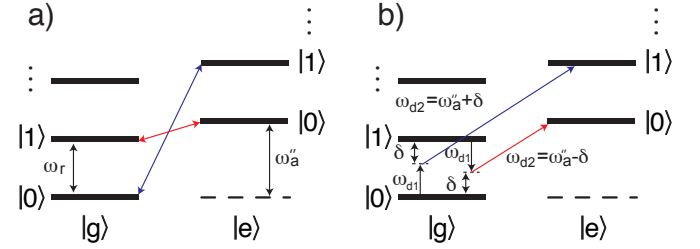


FIG. 6: (Color online) Red and blue sideband transitions. a) One-photon transitions. b) Two-photon transitions.

tions, respectively. Higher order transitions are neglected due to their small amplitudes. We rewrite these terms here in a more explicit form. This is done by going to a frame rotating at ω_r for the resonator and at the shifted frequency ω_{a_j}'' for the qubit, where

$$\omega_a'' = \omega_a + \frac{\Omega_{R_1}^2}{2\Delta_{a_1}} + \frac{\Omega_{R_2}^2}{2\Delta_{a_2}} + 2\frac{g^2}{\Delta'} \left(\langle a^\dagger a \rangle + \frac{1}{2} \right). \quad (7.4)$$

Here we keep the contribution of $\langle a^\dagger a \rangle$ to the frequency shift in order to take into account the presence of the measurement drive ε_3 . When evaluating $\langle a^\dagger a \rangle$, it is important to remember that, $a^{(\dagger)}$ is in the displaced frame defined in appendix B. Setting $\omega_{d_{k(\prime)}} = \omega_a'' + \omega_r$ the only term that does not average to zero due to rapid oscillations is the third line of Eq. (B10) which gives

$$H_{r1} = -cg \frac{\Omega_{R_k}}{\Delta_{a_k}} (\sigma_+ a + \sigma_- a^\dagger), \quad (7.5)$$

where $k = 1$ or 2 . Following the notation introduced in Sec. II A, we use $c = \cos \theta$ and $s = \sin \theta$ with θ the mixing angle. The above Hamiltonian corresponds to the one-photon red sideband transition. Alternatively, taking $\omega_{d_{k(\prime)}} = \omega_a'' - \omega_r$, we obtain the one-photon blue sideband transition

$$H_{b1} = -cg \frac{\Omega_{R_k}}{\Delta_{a_k}} (\sigma_+ a^\dagger + \sigma_- a). \quad (7.6)$$

On the other hand, the last line of (B10) will not average to zero if the drive frequencies are chosen such that

$$\omega_{d_k} \pm \omega_{d_{k'}} = \omega_a'' + \omega_r \quad (7.7)$$

or

$$2\omega_{d_{k(\prime)}} = \omega_a'' + \omega_r. \quad (7.8)$$

With these choices of drive frequencies, we obtain

$$H_{r2} = sg \frac{\Omega_{R_1}}{2\Delta_{a_1}} \frac{\Omega_{R_2}}{2\Delta_{a_2}} (\sigma_+ a + \sigma_- a^\dagger), \quad (7.9)$$

$$H_{b2} = sg \frac{\Omega_{R_1}}{2\Delta_{a_1}} \frac{\Omega_{R_2}}{2\Delta_{a_2}} (\sigma_+ a^\dagger + \sigma_- a).$$

corresponding to two-photon red and blue sideband transitions, respectively. These two-photon transitions are illustrated in Fig. 6b).

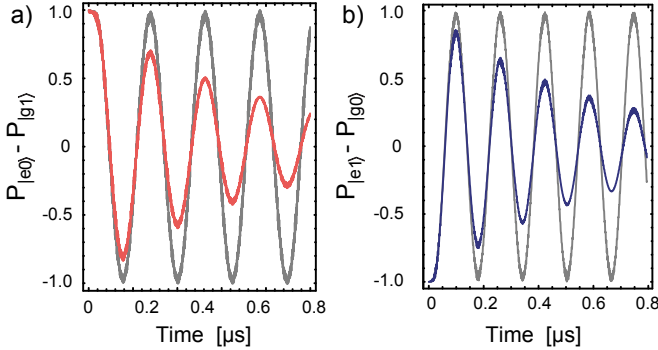


FIG. 7: (Color online) (a) Red and (b) blue coherent sideband oscillations. The system parameters are $\omega_a/2\pi = 7$ GHz, $\omega_r/2\pi = 5$ GHz, $g/2\pi = 100$ MHz. For the color curves, the damping is $\kappa/2\pi = 0.22$ MHz, $\gamma_1/2\pi = 0.02$ MHz and $\gamma_\phi/2\pi = 0.31$ MHz. These last two values are taken from the measured value reported in Ref. [3]. For the gray curves, damping was set to zero. The value of the drive frequencies and amplitudes are: a) $\omega_{d_1}/2\pi = 4593.59$ MHz, $\omega_{d_2}/2\pi = 6650.605$ MHz, $\varepsilon_1/2\pi = 841.91$ MHz and $\varepsilon_2/2\pi = 843.417$ MHz, b) $\omega_{d_1}/2\pi = 4598.39$ MHz, $\omega_{d_2}/2\pi = 7476.47$ MHz, $\varepsilon_1/2\pi = 1241.51$ MHz and $\varepsilon_2/2\pi = 1252.56$ MHz.

Because of the dependence of Eqs. (7.5) and (7.6) on the cosine of the mixing angle θ , the first order red and blue sideband transitions are forbidden at the charge degeneracy point. As discussed in appendix E, this can be linked to the symmetry of the Jaynes-Cummings Hamiltonian. Since it is more advantageous to work at the sweet spot to minimize dephasing, these first order transitions therefore appear to be of limited interest for coherent control in circuit QED. Moreover, since the frequencies corresponding to these first order transitions ($\omega_{a_j}'' \pm \omega_r$) are in practice very detuned from the resonator frequency ω_r , signals at these frequencies would be mostly reflected at the input port of the resonator. Very large input powers would therefore be required to compensate the attenuation.

On the other hand, because of their $\sin \theta$ dependence, the two-photon transitions have maximal amplitude at the sweet spot. Moreover, since in this case we require the sum or the difference of the drive frequencies to match the sideband conditions, these frequencies can be chosen such that there is minimal attenuation (while still avoiding measurement-induced dephasing [14, 16, 17]). However, the rate for these 2-photon transitions is of order $g \times (\Omega_R/2\Delta_a)^2$, which is g times the square of a small parameter. As is discussed in section VE, obtaining large rates will require large coupling strength g .

To realize logical gates based on the red and blue sidebands, these transitions must be coherently driven. The corresponding simulated coherent oscillations are illustrated in Figure 7 for the two-photon red (a) and blue (b) sideband transitions. In these numerical calculations, the drive frequency ω_{d_1} is chosen ~ 400 MHz away from the resonator frequency to avoid measurement-induced dephasing of the qubit. In a first step, the second drive fre-

quency ω_{d_2} is then chosen using the condition of Eq. (7.7). Using simulated annealing [49], the drive frequencies and the corresponding drive amplitudes $\varepsilon_{1(2)}$ are then varied to optimize the fidelity of the sideband transitions. The best (but not necessarily optimal) values obtained are given in the caption of Fig. 7. Using these parameters, we obtain a population transfer of 0.83 for the red sideband and of 0.86 for the blue sideband (without damping, we obtain near perfect population transfer of 1.0 in both cases). This relatively low population transfer is essentially due to the small dephasing time $1/\gamma_2 = 500$ ns used here with respect to the slow rate ~ 5 MHz of the red and blue sideband transitions. It is interesting to point out that this value of the rate is about 4 times bigger than expected from the perturbative estimates of Eq. (7.9). These estimates should be taken as lower bounds which can be improved by numerical optimisation.

C. One-photon sidebands at the sweet spot using ac-dither

In the previous section, we saw that the symmetry of the circuit QED Hamiltonian does not allow for first order red and blue sideband transitions at the charge degeneracy point. However, with ac-dither discussed in section III D, it is possible to take advantage of the small gate charge excursions away from the sweet spot to obtain a one-photon transition while staying, on average, at the sweet spot. This can be seen as a low frequency version of the two-photon transitions.

To analyse this situation, we focus on a single qubit coupled to the resonator and in the presence of a single coherent drive of amplitude ε and frequency ω_d . At the charge degeneracy point ($n_g^{\text{dc}} = 1/2$) and with ac-dither on the voltage port, we get for the Hamiltonian:

$$H = \omega_r a^\dagger a + \frac{E_J}{2} \sigma_z + \frac{A}{2} \cos(\omega_{\text{act}} t) \sigma_x + g (2n_g^{\text{ac}} \cos(\omega_{\text{act}} t) + \sigma_x) (a^\dagger + a) + \varepsilon (a^\dagger e^{-i\omega_d t} + a e^{+i\omega_d t}), \quad (7.10)$$

where we have defined $A = 8E_C n_g^{\text{ac}}$ and have taken the ac-gate bias to be $n_g^{\text{ac}} \cos(\omega_{\text{act}} t)$. Assuming that the dither frequency is small with respect to the qubit transition frequency but large compared to the coupling strength, $g \ll \omega_{\text{act}} \ll \omega_a$, we move to the adiabatic basis to obtain

$$H = \omega_r a^\dagger a + \frac{\omega_a^{\text{ad}}(t)}{2} \tilde{\sigma}_z + \varepsilon (a^\dagger e^{-i\omega_d t} + a e^{+i\omega_d t}) + g [2n_g^{\text{ac}} \cos(\omega_{\text{act}} t) + \sin \Theta(t) \tilde{\sigma}_z + \cos \Theta(t) \tilde{\sigma}_x] (a^\dagger + a), \quad (7.11)$$

where $\omega_a^{\text{ad}}(t) = [E_J^2 + A^2 \cos^2(\omega_{\text{act}} t)]^{1/2}$ is the instantaneous qubit transition frequency.

Comparing with Eq. (2.3), we have the following map-

ping

$$\mu \mapsto -2n_g^{ac} \cos(\omega_{ac}t), \quad c \mapsto \sin \Theta(t), \quad s \mapsto -\cos \Theta(t) \quad (7.12)$$

and it is possible to use directly all of the results obtained in the previous section. The important point is that we now get a $\tilde{\sigma}_z$ component even at the charge degeneracy point, which means that the red and blue sidebands will be allowed to first order. This is due to the small excursions away from degeneracy provided by the ac-dither.

Assuming that the dither amplitude is small with respect to the bare qubit transition frequency E_J , we take $\Theta(t) \approx A \cos(\omega_{ac})/E_J$ which will yield simple Bessel function FM modulation sidebands for the qubit transition. Following section III D and using the results of the previous section, we get the blue sideband transition for $\omega_d = \omega_a'' + \omega_r \pm \omega_{ac}$

$$H_{b1_{ac}} = g \left(\frac{\Omega_R}{2\Delta_a} \right) J_1 \left(\frac{8E_C n_g^{ac}}{E_J} \right) (a^\dagger \tilde{\sigma}_+ + a \tilde{\sigma}_-), \quad (7.13)$$

and for $\omega_d = \omega_a'' - \omega_r \pm \omega_{ac}$ the red blue sideband transition

$$H_{r1_{ac}} = g \left(\frac{\Omega_R}{2\Delta_a} \right) J_1 \left(\frac{8E_C n_g^{ac}}{E_J} \right) (a \tilde{\sigma}_+ + a^\dagger \tilde{\sigma}_-). \quad (7.14)$$

Here we have focused on the first dither sideband $J_1(z)$ only. With respect to the two-photon transitions of Eq. (7.9), we have simply replaced a factor of $\Omega_R/2\Delta_a$ by the ac-sideband modulation $J_1(8E_C n_g^{ac}/E_J)$. Both of these quantities are smaller than unity, so whether this is advantageous depends on the parameters of the system. As an example, taking $E_C \sim 5$ GHz, $E_J \sim 6$ GHz [16], and a 10% of 2e excursion for the dither, $n_g^{ac} = 0.1$, we have $J_1(8E_C n_g^{ac}/E_J) \sim 3/10$.

D. CNOT from sideband transitions

In this section, we show how to obtain non-trivial two-qubit gates from red and blue sideband transitions. This is included for completeness, with most of the results already known from Cirac and Zoller [35] for three level atoms and from Childs and Chuang [36] for two level atoms. Here, we follow closely the results and notation of Ref. [36].

Following Ref. [36], we introduce the unitary operators [57]

$$R_j^+(\theta, \phi) = \exp \left[-i \frac{\theta}{2} (e^{-i\phi} a^\dagger \sigma_{+j} + e^{+i\phi} a \sigma_{-j}) \right], \quad (7.15)$$

$$R_j^-(\theta, \phi) = \exp \left[-i \frac{\theta}{2} (e^{-i\phi} a^\dagger \sigma_{-j} + e^{+i\phi} a \sigma_{+j}) \right]. \quad (7.16)$$

$R_j^+(\theta, \phi)$ corresponds to a pulse on the blue-sideband for qubit j and $R_j^-(\theta, \phi)$ the red-sideband. Here, ϕ is the phase of the driving field.

In addition to the above resonator-qubit operations, we introduce the single-qubit unitary operators corresponding to the effective Hamiltonians discussed in section III. We denote the single qubit flip (x) and phase (z) operators acting on qubit j as:

$$R_j^x(\theta) = \exp \left[-i \frac{\theta}{2} \sigma_{xj} \right], \quad R_j^z(\theta) = \exp \left[-i \frac{\theta}{2} \sigma_{zj} \right], \quad (7.17)$$

Another useful single qubit unitary is the Hadamard transformation (in the basis $\{|e\rangle, |g\rangle\}$)

$$H_j = \frac{1}{\sqrt{2}} \begin{pmatrix} 1 & 1 \\ 1 & -1 \end{pmatrix}, \quad (7.18)$$

which can be obtained by a rotation at an angle between the x and z axis or, equivalently, by a sequence of one-qubit gates

$$H_j = \exp \left[-i \frac{\pi}{2} \left(\frac{\sigma_{xj} + \sigma_{zj}}{\sqrt{2}} \right) \right] = R_j^x(\pi/2) R_j^z(\pi/2) R_j^x(\pi/2). \quad (7.19)$$

Before building a universal two-qubit gate from these elementary operations, we first discuss a simpler protocol to create conditional entanglement. This protocol is based on Ref. [50] and relies on entangling one qubit to the resonator and then transferring the entanglement to qubit-qubit correlations. This is realized by the sequence

$$R_1^-(\pi, \phi) R_2^-(\pi/2, \phi) R_1^-(\pi, \phi), \quad (7.20)$$

where the phase ϕ is arbitrary. It is simple to verify that this sequence will leave $|gg0\rangle$ unchanged but will create maximally entangled states when starting from $|ge0\rangle$ or $|eg0\rangle$. However, the state $|ee0\rangle$ will irreversibly leak out of the $\{|0\rangle, |1\rangle\}$ photon subspace and the qubits will get entangled with the resonator at the end of the pulse sequence. Hence, while (7.20) is not an universal two-qubit primitive, it can nevertheless be used to generate conditional entanglement. This sequence can also be realized with all blue sideband pulses. In this case, $|ee0\rangle$ is left unchanged while starting with $|gg0\rangle$ will create spurious entanglement with the resonator.

In the above sequence, the spurious entanglement occurs in the second step where the initial state $|ee0\rangle$ picks up a contribution from the two-photon state $|gg2\rangle$. For this state, the evolution is “faster” by a factor of $\sqrt{2}$ from evolution in the one-photon subspace. Because of this, the last step in the sequence cannot completely undo the qubit-resonator entanglement and leaves them partially entangled. To solve this problem, Childs and Chuang [36] introduced the qubit-resonator gate

$$P_j = R_j^+(-\pi/2, 0) R_j^+(\pi\sqrt{2}, -\pi/2) R_j^+(-\pi/2, 0). \quad (7.21)$$

In the basis $\{|e0\rangle, |e1\rangle, |g0\rangle, |g1\rangle\}$, P_j takes the form $P_j = \text{diag}(1, e^{-i\pi/\sqrt{2}}, e^{i\pi/\sqrt{2}}, -1)$. This gate entangles the qubit with the resonator (because of the minus sign

in the last element) but it does not lead to leakage into higher photon states. Using this gate, Childs and Chuang [36] proposed a sequence of red, blue and single-qubit operations that generates a CNOT gate.

Here, building on Eq. (7.20), we note a simpler entangling two-qubit gate (in the basis $\{|ee\rangle, |eg\rangle, |ge\rangle, |gg\rangle\}$)

$$\begin{aligned} U_\varphi &= R_1^+(\pi, \phi) P_2 R_1^+(\pi, \phi) \\ &= \text{diag}(1, e^{i\pi/\sqrt{2}}, -e^{-i\pi/\sqrt{2}}, 1). \end{aligned} \quad (7.22)$$

Using this gate, it is possible to obtain a CNOT gate which relies only on single qubit unitaries and blue-sideband transitions:

$$\text{CNOT} = R_1^z([1 + \sqrt{2}]\pi) H_2 U_\varphi R_2^z(-\pi/\sqrt{2}) H_2. \quad (7.23)$$

Because it relies on P_j , this gate does not lead to unwanted qubit-resonator entanglement.

E. Summary

The gates presented in this section rely on real excitations of the resonator to mediate entanglement between the qubits. These gates are based on perturbation theory and are therefore relatively slow. For example, for the red and blue sideband oscillations studied in section VII B, we have found after numerical optimization rates of ~ 5 MHz. With a dephasing time of 500 ns, this corresponds to a quality factor of about 9, larger than what was expected from perturbation theory. While this quality factor is not large enough for large scale quantum computation, it is certainly enough to demonstrate the concept experimentally.

Finally, a disadvantage of the gates based on real excitation of the resonator is that they are susceptible to photon loss and therefore require relatively large Q resonators. This conflicts with the requirement of fast readout.

VIII. GEOMETRIC PHASE GATE

The gates discussed in the previous sections were based on real or virtual transitions. In the present section, we discuss a different approach, based on the geometric phase. This was already discussed in the context of ion-trap quantum computing [25, 26]. This gate is based on the first term of the second line of the Hamiltonian (B10):

$$\tilde{H} = - \sum_{j=1,2} g_j B_j \sigma_{z_j} (a^\dagger + a), \quad (8.1)$$

where B_j is given by Eq. (B9). Here, we work at the charge degeneracy point where $c_{1,2} = 0$. Although the Hamiltonian (8.1) does not couple the qubits directly, it couples both qubits to the resonator field a . By using a time dependent drive on the resonator, and hence displacing the field a in a controlled manner, it is possible

to induce indirect qubit-qubit coupling without residual entanglement with the field.

To see this explicitly, we first rederive the effective Hamiltonian (8.1) in the presence of a single drive of frequency ω and of amplitude $\varepsilon(t)$. Here, we allow the amplitude to be time-dependent and complex. Moreover, we will assume that the qubits are detuned from each other ($\omega''_{a_1} \neq \omega''_{a_2}$) such that the flip-flop interaction can be neglected and that both qubits are dispersively coupled to the resonator. In a frame rotating at the resonator frequency ω_r , we obtain

$$\tilde{H}(t) \approx \frac{1}{2} \sum_{j=1,2} \left(\omega''_{a_j}(t) + 2f_j(t)a^\dagger + 2f_j^*(t)a \right) \sigma_{z_j}, \quad (8.2)$$

where

$$\begin{aligned} f_j(t) &= g_j^2 e^{-i\Delta_j t} \int_0^t \int_0^{t'} dt' dt'' e^{i(\Delta_j + i\kappa/2)t'} e^{i(\Delta_r - i\kappa/2)t''} \varepsilon(t''). \end{aligned} \quad (8.3)$$

Because of the time dependent drive, the shifted qubit transition frequencies $\omega''_{a_j}(t)$ are now time-dependent. Note that, following the procedure of appendix A, we have added the effect of cavity damping κ to Eq. (8.3).

Since

$$\begin{aligned} &[\tilde{H}(t_1), \tilde{H}(t_2)] \\ &= 2i(\text{Im}[f_1^*(t_1)f_2(t_2)] + \text{Im}[f_2^*(t_1)f_1(t_2)]) \sigma_{z_1} \sigma_{z_2} \quad (8.4) \\ &\equiv 2iF(t_1, t_2) \sigma_{z_1} \sigma_{z_2} \end{aligned}$$

commutes with $\tilde{H}(t)$ for all times, evolution under the effective Hamiltonian (8.2) is given by

$$U(T, 0) = e^{-i \int_0^T dt \tilde{H}(t)} e^{-\frac{1}{2} \int_0^T \int_0^t dt dt' [\tilde{H}(t), \tilde{H}(t')]} \quad (8.5)$$

To avoid unwanted entanglement of the qubits with the resonator at the final gate time T , we choose the time-dependent drive amplitude $\varepsilon(t)$ such that [25, 26]

$$\int_0^T dt f_j(t) = 0. \quad (8.6)$$

With this choice of $\varepsilon(t)$, evolution under $\tilde{H}(t)$ corresponds to the application of a local phase shift

$$\phi_j(T) = \int_0^T dt \omega''_{a_j}(t) \quad (8.7)$$

to each qubit and of a conditional phase shift $\exp[-i\Phi_{12}(t)\sigma_{z_1}\sigma_{z_2}/2]$ where

$$\Phi_{12}(T) = 2 \int_0^T \int_0^t dt dt' F(t, t'). \quad (8.8)$$

For $\Phi_{12}(T) = \pm\pi/2$, this two-qubit operation is known to be equivalent to the CNOT gate, up to one qubit gates.

Our goal is therefore to choose the drive $\varepsilon(t)$ such that the qubits accumulate a phase $\Phi_{12}(T) = \pm\pi/2$ in the smallest time T possible. This minimization has to take into account several constraints. In addition to (8.6), we take the drive to be off at the start and at the end of the gate:

$$\varepsilon(0) = \varepsilon(T) = 0. \quad (8.9)$$

The assumption that the drive is initially turned off is already built into our expression for $f_j(t)$ in Eq. (8.3). To prevent further phase accumulation after the gate time T , we also require that

$$\alpha(T) = 0, \quad (8.10)$$

$$\dot{\alpha}(T) = 0, \quad (8.11)$$

where $\alpha(t)$ is the amplitude of the classical field inside the resonator and is given by Eq. (3.4) [or Eq. (A5) in presence of cavity damping]. From Eq. (3.4), we have that $\dot{\alpha}(T) = 0$ will be automatically satisfied if Eqs. (8.9) and (8.10) are satisfied.

While satisfying the above constraints, the external field $\varepsilon(t)$ must also be chosen such that the approximation that led to Eqs. (8.2) and (8.3) are valid. There are two approximations. The first one, as in Section III B, is that we adiabatically eliminated transitions in the qubit caused by the external drive. This requires the drive to be either of small amplitude or sufficiently detuned from the qubits. The second approximation is the dispersive transformation, which here only has the effect of

renormalizing the qubit transition frequency ω_{aj}'' . This approximation breaks down on a scale given by the critical photon number $n_{\text{crit}} = \Delta^2/4g^2$ [14, 17]. We must therefore choose the drive amplitude and frequency such that the resonator never gets populated by more than n_{crit} photons. Beyond this number, additional mixing between the qubits and resonator states is possible and would likely lead to unwanted qubit-resonator entanglement [58]

Finally, we also require that the measurement-induced dephasing time of the qubits due to the control drive, the gate-induced dephasing time, to be smaller than the ‘intrinsic’ dephasing time T_2 . An expression for the measurement-induced dephasing rate is given in Eq. (3.12). Here, we will use Eq. (5.16) of Ref. [17] that is more appropriate for a time-dependent drive. As was discussed in section III C and in Ref. [17], by working at sufficiently large detuning Δ_r , gate-induced dephasing can be made negligible while still maintaining a large rate for the gates.

It is useful to take into account these constraints by developing the pulse envelope $\varepsilon(t)$ in Fourier components

$$\varepsilon(t) = \sum_{n=-\infty}^{\infty} c_n e^{i\omega_n t}. \quad (8.12)$$

Using this expression, we rewrite $f_j(t)$ as

$$\begin{aligned} f_j(t) &= g_j^2 \sum_{n=-\infty}^{\infty} c_n \left\{ \frac{-e^{i(\Delta_r + \omega_n)t}}{(\Delta_j + \Delta_r + \omega_n)(\Delta_r + \omega_n - i\kappa/2)} + \frac{e^{-\kappa t/2}}{(\Delta_j + i\kappa/2)(\Delta_r + \omega_n - i\kappa/2)} + \frac{-e^{-i\Delta_j t}}{(\Delta_j + \Delta_r + \omega_n)(\Delta_j + i\kappa/2)} \right\} \\ &\approx -\chi_j \sum_{n=-\infty}^{\infty} c_n \frac{e^{i(\Delta_r + \omega_n)t} - e^{-\kappa t/2}}{(\Delta_r + \omega_n - i\kappa/2)} \end{aligned} \quad (8.13)$$

where we have assumed the resonator-qubit detuning Δ_j is large, such that $\Delta_j \gg \{\Delta_r + \omega_n, \kappa/2\}$, and have dropped the small and fast oscillating last term in the second expression. This approximate expression will be useful in obtaining analytical estimates for the expected gate time T .

Using the approximate expression for $f_j(t)$, we can now recast the above constraints in more simple forms. Using (8.13), the no-effect on the resonator constraint of

Eq. (8.6) can be written as

$$\begin{aligned} \int_0^T dt f_j(t) &\approx -\chi_j \sum_{n=-\infty}^{\infty} c_n \int_0^T dt \frac{e^{i(\Delta_r + \omega_n)t} - e^{-\kappa t/2}}{(\Delta_r + \omega_n - i\kappa/2)} \\ &= \chi_j \sum_{n=-\infty}^{\infty} c_n A_n = 0. \end{aligned} \quad (8.14)$$

Without the approximation for $f_j(t)$, the coefficient A_n depends on the qubit index j which means that there would be one extra constraint to satisfy.

Moreover, to satisfy Eq. (8.9), we take $\omega_n = 2\pi n/T$

which implies that

$$\varepsilon(0) = \varepsilon(T) = \sum_{n=-\infty}^{\infty} c_n = 0. \quad (8.15)$$

To satisfy Eq. (8.10), we have

$$\begin{aligned} \alpha(T) &= \sum_{n=-\infty}^{\infty} c_n \frac{e^{i(\Delta_r + \omega_n)T} - e^{-\kappa T/2}}{(\Delta_r + \omega_n - i\kappa/2)} \\ &\equiv \sum_{n=-\infty}^{\infty} c_n B_n = 0. \end{aligned} \quad (8.16)$$

Casting, in a simple form, the constraints that there is not qubit transition and that the dispersive approximation holds is more difficult. For the former case, we require that

$$|f_j(t)e^{-i\Delta_r t}/g_j| \sim \left| \frac{g_j \varepsilon(t)}{\Delta_j \Delta_r} \right| \quad (8.17)$$

be smaller than about 1/10 for all time. In terms of the drive amplitude we thus require

$$|\varepsilon(t)| \lesssim \left| \frac{\Delta_j \Delta_r}{10g_j} \right|. \quad (8.18)$$

Finally, for the dispersive approximation to hold, we require that the average photon number populating the resonator be no larger than the critical photon number:

$$\bar{n} \approx \frac{\varepsilon^2}{\Delta_r^2} \sim \frac{\Delta_j^2}{4g_j^2} \quad (8.19)$$

or, equivalently,

$$|\varepsilon(t)| \lesssim \left| \frac{\Delta_j \Delta_r}{2g_j} \right|. \quad (8.20)$$

In practice, we therefore only have to deal with Eq. (8.18) and only with the qubit for which $|\Delta_j/g_j|$ is smallest. In the dispersive regime and in the $\kappa = 0$ approximation, we thus require $|\varepsilon(t)| \lesssim \Delta_r$ which means that there is no gate effect at $\Delta_r \rightarrow 0$.

Of all the constraints, the last one is the most difficult to deal with because it must hold at all intermediate times t and because it involves the absolute value of the complex drive amplitude $\varepsilon(t)$. It is nevertheless possible to find an analytical expression for the gate time T by developing on four Fourier components $\{c_{-1}, c_0, c_1, c_2\}$. In this situation, all constraints can be solved for analytically and it is possible to find an expression for the gate time. This expression is however unsightly and we only give here relevant limits. In the situation where Δ_r is large, we find that

$$T \sim \frac{\pi |\Delta_r|}{\chi_1 \chi_2}. \quad (8.21)$$

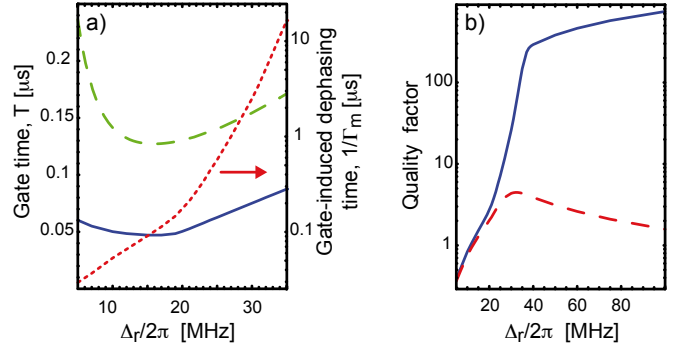


FIG. 8: (Color online) a) Gate time (full blue and green dashed) and gate-induced dephasing (red dotted) as a function of detuning Δ_r . The green dashed line is obtained analytically by decomposing the pulse $\varepsilon(t)$ over four Fourier coefficients and using the constraints derived from the approximate expression in Eq. (8.13). The full blue line is obtained numerically by using the constraints derived from the exact expression in Eq. (8.13) and decomposing over 5 Fourier coefficients. The dotted red line is the gate-induced dephasing time as calculated from Ref. [17] and presented on a log scale. The system parameters used are given in the text. b) Quality factor of the geometric phase gate as a function of detuning. The red dashed line takes into account gate-induced dephasing and an additional T_2 of 500 ns. For the full blue line, we have taken $1/T_2 = 0$. Clearly, gate-induced dephasing is not a limitation in practice.

In the dispersive approximation this is roughly given by $T \sim 100\pi|\Delta_r|/g^2$. In the small Δ_r limit we rather find that $T \propto 1/|\Delta_r|$. As explained above, this behavior is expected from Eq. (8.18) which is saying that the field amplitude goes to zero at zero detuning in the $\kappa = 0$ limit. The full expression for T as a function of detuning Δ_r is plotted in Fig. 8a) [dashed green line]. The system parameters used here are $g_1/2\pi = g_2/2\pi = 100$ MHz, $\Delta_1/2\pi = 1$ GHz and $\Delta_2/2\pi = 1.1$ GHz. The approximate expression for T at large Δ_r is of similar form to that already obtained for gates based on the dispersive approximation: a rate equal approximately to the square of the coupling g over a detuning. Here however the detuning is Δ_r and not the qubit-resonator detuning Δ . In the dispersive approximation, the former can however be made much smaller than the latter and this gate could in principle be faster than the dispersive based gates discussed in the previous sections.

Going beyond the assumptions made to obtain the approximate expression for $f_j(t)$ in Eq. (8.13), we solved numerically the optimization problem. Without this approximation there are now five constraints to optimize over [the constraint Eq. (8.14) now has to be satisfied independently for both qubits] and thus a minimum of five Fourier coefficients have to be used. The full blue line in Fig. 8a) shows the numerically found gate time as a function of detuning and using the same system parameters as given above. As can be seen from this figure, going beyond the approximations used to get an analytical es-

timate and increasing the number of Fourier components improved significantly the gate time. In this situation, we get an optimal gate time of $T \sim 50$ ns. Further optimisation can be made by increasing the coupling strength, and could likely be made by increasing the number of Fourier components.

Figure 8a) also shows the gate-induced dephasing time [dotted red line] associated with the pulse required to implement the geometric phase gate. This dephasing time is obtained from Eq. (5.16) of Ref. [17] and assuming a resonator damping rate of $\kappa/2\pi = 0.1$ MHz. At detunings larger than about $\Delta_r/2\pi \sim 25$ MHz, the measurement-induced dephasing time is significantly larger than the ‘intrinsic’ T_2 of 500 ns already measured in circuit QED [3] and can thus be ignored. However, this induced dephasing time goes down rapidly with detuning such that there is a detuning ($\Delta_r/2\pi \sim 10$ MHz with the chosen parameters) below which it is smaller than the gate time, meaning that the geometric phase gate cannot be used.

Figure 8b) shows the quality factor, as defined by Eq. (3.14) and where the dephasing rate was taken to be the sum of the gate-induced dephasing rate and of the ‘intrinsic’ dephasing rate $1/T_2$. For the red dashed line, we have taken $T_2 = 500$ ns, while T_2 was set to infinity for the full blue line. For $T_2 = 500$ ns and the present system parameters, the quality factor is maximum for detunings of about 30 MHz. However, as is clear from the full blue line, gate-induced dephasing time is not a limitation in practice and the quality factor could be significantly better once T_2 is improved in this system and by working at larger detunings. Moreover, the actual magnitude of the quality factor could likely be improved by increasing the number of Fourier components. We also point out that the present results have been obtained within the approximations used to derive the effective Hamiltonian of Eq. (8.2). Significant improvements could be made by numerically optimizing the full system’s master equation. In this case, the results would not be limited by the dispersive approximation used here and we expect a much better quality factor.

Finally, it is important to realize that whenever two qubits are present in the resonator and the system is being driven, this geometric gate is in action. This could lead to unwanted qubit-qubit entanglement and, since Eq. (8.6) might not be satisfied, qubit-resonator entanglement if the drive amplitude and frequency are not chosen appropriately.

IX. CONCLUSION

We have explored the realization of single and two-qubit gates in circuit QED, using realistic systems parameters. We have shown how all single-qubit rotations can be realised with minimal measurement-induced dephasing of the qubit. In this context, two approaches to change the qubit transition frequency without dc bias

away from the sweet spot were discussed. Both rely on off-resonant irradiation of the qubit. Interestingly, the ac-dither approach could help in reducing dephasing by protecting the qubit from low-frequency noise.

Five types of two-qubit gates were discussed. The fastest gate discussed in this paper is based on direct coupling of qubits with the resonator. In this paper however, we have focused on gates requiring no dc-bias away from the sweet spot or additional control lines not present in the current circuit QED architecture. These gates can in practice be slower but could be implemented in the current circuit QED design, without additional design elements. Moreover, these gates have the important advantage that they do not cause extra dephasing of the qubits by moving away from the sweet spot.

The rates and quality factors for these gates, as obtained from perturbation theory, are summarized in Table I. These are given for $g/2\pi = 100$ MHz and $\kappa/2\pi = 0.1$ MHz (‘current’) and $g/2\pi = 200$ MHz and $\kappa/2\pi = 0.01$ MHz (‘better’). All other parameters are equal and discussed in the table caption. These parameters correspond to already realised values and to realistic values that could be obtained in future realizations of circuit QED, respectively. The quality factors are calculated in the same way as in Eq. (3.14): the rates divided by $2T_2^{-1}$ (the full width at half-maximum of the qubit spectral line). However, for the direct coupling and the sidebands, the loss of a single photon has a large impact and the quality factors are therefore given by the rates divided by the mean of the two contributing decay channels: $(\kappa + 2T_2^{-1})/2$. For the geometric phase gate, the ‘current’ quality factor, and the corresponding rate, are taken from the inset of Fig. 8. The ‘better’ results are obtained from a similar calculation.

Moreover, we note that the same values of T_2 and κ were used for the direct coupling gate requiring dc excursions away from the sweet spot and the other gates that do not require such excursions. As discussed before, it is likely that T_2 or κ would be reduced due to the direct tuning. The rates and quality factors given on the first line of the table can therefore be taken as upper bounds.

It is also important to realise that, apart from the first line of the table, these results have been obtained by perturbation theory and are thus *lower bounds* on the rates and quality factors that can be obtained in practice. Better results can be obtained from numerical optimization. This was already shown in Fig. 7 for the red and the blue sideband and also in section VIII for the geometric phase. Therefore, there is good hope that all of the gates discussed in this paper could be realized experimentally, admittedly with different degree of usefulness for quantum information processing. Moreover, all the quality factors quoted in table I are limited by the system’s decoherence time T_2 and not by measurement-induced dephasing rate from the application of the gate. As a result, increasing T_2 in this system will lead to significantly better quality factors.

The key to improve the gate’s quality factor is to im-

	Rates	Rates (current)	Q (current)	Rates (better)	Q (better)
§IV Direct coupling	g	$\lesssim 100$	$\lesssim 272$	$\lesssim 200$	$\lesssim 619$
§V Virtual interaction	g^2/Δ	~ 10	~ 16	~ 20	~ 31
§VII B Red/Blue sideband	$g(\Omega_{R_1}/2\Delta_{a_1})(\Omega_{R_2}/2\Delta_{a_2})$	> 1	> 3	> 2	> 6
§VII C Red/Blue sideband (ac-dither)	$g(\Omega_R/2\Delta_a)J_1(8E_C n_g^{ac}/E_J)$	> 3	> 8	> 6	> 19
§VIII Geometric phase	$> g^2/200\Delta_r$	> 3	> 4	> 6	> 9

TABLE I: Rates and quality factors of the various gates. For the direct coupling gate, the values presented are upper bounds. For the sidebands and geometric phase gates the results presented are only *lower bounds*. The system parameters are taken as $g/\Delta = 0.1 = \Omega_R/2\Delta_a = 0.1$ for the approximations used to derive the rates to be valid. For the ‘current’ results, we have taken $g/2\pi = 100$ MHz and $\kappa/2\pi = 0.1$ MHz. For the ‘better’ results, we have taken $g/2\pi = 200$ MHz and $\kappa/2\pi = 0.01$ MHz. The dephasing time was taken as $T_2 = 500$ ns, as measured in Ref. [3] in this system. For the geometric phase, we took $\varepsilon = \Delta_r$ to satisfy both Eq. (8.18) and the dispersive approximation. For the “current” results, we have taken $\Delta_r/2\pi = 32$ MHz and for the “better” results $\Delta_r/2\pi = 70$ MHz.

prove the coupling coupling g and the resonator and qubit relaxation and dephasing times. Since the first circuit QED experiment [15], g as been improved by almost a factor of 20 and further improvements can be realized without technical challenges. Resonators with long photon lifetimes, in the tens of microseconds, have already been fabricated [29] and first steps in the design and realization of a new charge-type qubit which is largely insensitive to charge noise have been taken [18]. Circuit QED therefore seem like a promising system with which to study quantum mechanics at the large scales and quantum information processing.

Acknowledgments

The authors are very grateful to Yale CQuIP visitor Peter Zoller for helpful discussions concerning the geometric phase gate and its mapping to circuit QED. This work was supported in part by the Army Research Office and the National Security Agency through grant W911NF-05-1-0365, the NSF under grants ITR-0325580, DMR-0342157 and DMR-0603369, and the W. M. Keck Foundation. AB was partially supported by the Natural Sciences and Engineering Research Council of Canada (NSERC), the Fond Québécois de la Recherche sur la Nature et les Technologies (FQRNT) and the Canadian Institute for Advanced Research (CIAR).

APPENDIX A: FIELD DISPLACEMENT ON THE MASTER EQUATION

In this appendix, we apply the field displacement procedure of section III on the the master equation (2.5) rather than on the pure state evolution. Since the displacement is on the resonator field, we only consider the contribution to damping due to κ . The master equation thus reads

$$\dot{\rho} = -i[H, \rho] + \frac{\kappa}{2} (2a\rho a^\dagger - a^\dagger a\rho - \rho a^\dagger a), \quad (A1)$$

where

$$H = \omega_r a^\dagger a + \frac{\omega_a}{2} \sigma_z - g (a^\dagger \sigma_- + \sigma_+ a) + \sum_k (\varepsilon_k(t) a^\dagger e^{-i\omega_{d_k} t} + \varepsilon_k^*(t) a e^{+i\omega_{d_k} t}). \quad (A2)$$

For simplicity of notation, in this appendix we only consider a single qubit and drop the j index. Going to the displaced frame, the master equation for the displaced density matrix $\tilde{\rho} = D^\dagger(\alpha)\rho D(\alpha)$ reads

$$\begin{aligned} \dot{\tilde{\rho}} &= -i[D^\dagger(\alpha)H D(\alpha), \tilde{\rho}] - D^\dagger(\alpha)\dot{D}(\alpha)\tilde{\rho} - \tilde{\rho}\dot{D}^\dagger(\alpha)D(\alpha) \\ &\quad + \frac{\kappa}{2} D^\dagger(\alpha) (2a\rho a^\dagger - a^\dagger a\rho - \rho a^\dagger a) D(\alpha) \\ &= -i[\tilde{H}, \tilde{\rho}] + \frac{\kappa}{2} (2a\tilde{\rho} a^\dagger - a^\dagger a\tilde{\rho} - \tilde{\rho} a^\dagger a) \end{aligned} \quad (A3)$$

where

$$\begin{aligned} \tilde{H} &= \omega_r a^\dagger a + \frac{\omega_a}{2} \sigma_z - g (a^\dagger \sigma_- + \sigma_+ a) \\ &\quad - g (\alpha^* \sigma_- + \alpha \sigma_+) \end{aligned} \quad (A4)$$

and the parameter α is chosen to satisfy

$$\dot{\alpha} = -i\omega_r \alpha - i \sum_k \varepsilon_k e^{-i\omega_{d_k} t} - \frac{\kappa}{2} \alpha. \quad (A5)$$

As an example, we consider the simple case of the bit-flip gate discussed in section III A. In this situation, a single time-independent and real drive ε is needed. With $\alpha(0) = 0$ and dropping the transient term, we recover the Hamiltonian (3.5) where the Rabi rate now reads

$$\Omega_R = 2 \frac{g\varepsilon}{\Delta_r - i\kappa/2}. \quad (A6)$$

As it should, this rate does not diverge at $\Delta_r = 0$. Since we always work in the regime where Δ_r is large, we neglect this κ correction in most sections of this paper.

APPENDIX B: DERIVATION OF THE EFFECTIVE HAMILTONIAN

In this appendix we derive an effective Hamiltonian for two qubits dispersively coupled to a single resonator and taking into account the presence of three independent drives. Two of these drives ($k = 1, 2$) are used to coherently control the qubits while the third drive ($k = 3$) plays the role of measurement beam. Our starting point is Hamiltonian (2.3) taking into account the gate charge dependence. While working away from charge degeneracy is not useful in practice, this will make selection rules appear clearly.

The derivation follows the same steps as those presented in section III. For simplicity, we take the drive amplitudes ε_k to be time-independent. This assumption is relaxed in the context of the geometric phase gate in section VIII. As in section III, we start by displacing the resonator field a by using the displacement operator $D(\alpha)$. Since ε_3 plays the role of measurement, its frequency will be close to the resonator frequency ω_r . It is therefore more convenient to displace the field only with respect to the first two drives. In the lab frame, the result of this transformation is

$$\begin{aligned} H^{(1)} = & \omega_r a^\dagger a + \frac{\omega_{a_1}}{2} \sigma_{z_1} + \frac{\omega_{a_2}}{2} \sigma_{z_2} + \varepsilon_3 (a^\dagger e^{-i\omega_{d_3}t} + \text{h.c.}) \\ & - \sum_{j=1,2} g_j (\mu_j - c_j \sigma_{z_j} + s_j \sigma_{x_j}) (a^\dagger + a) \\ & + \sum_{j,k=1,2} \Omega_{R_{jk}} (c_j \sigma_{z_j} - s_j \sigma_{x_j}) \cos(\omega_{d_k} t), \end{aligned} \quad (\text{B1})$$

where $\Omega_{R_{jk}} = 2g_j \varepsilon_k / (\omega_r - \omega_{d_k})$ is the Rabi frequency of qubit j with respect to drive k .

In the next step, we make the rotating wave approximation on the drive terms acting on the qubits [last term of Eq. (B1)]:

$$\begin{aligned} & \sum_{j,k=1,2} \Omega_{R_{kj}} (c \sigma_{z_j} - s \sigma_{x_j}) \cos(\omega_{d_k} t) \\ & \approx \sum_{j,k=1,2} s_j \frac{\Omega_{R_{kj}}}{2} (\sigma_{+j} e^{-i\omega_{d_k}t} + \sigma_{-j} e^{+i\omega_{d_k}t}). \end{aligned} \quad (\text{B2})$$

Not doing this approximation would only lead to small Bloch-Siegert shifts in the qubit transition frequency [51].

In this appendix, we are not interested in direct transitions of the qubits (i.e single-qubit Rabi flopping), these transitions are therefore eliminated using the transformation of Eq. (3.10) on each qubit:

$$U_j = \exp [\beta_j^* \sigma_{+j} - \beta_j \sigma_{-j}]. \quad (\text{B3})$$

Since $[U_1, U_2] = 0$, these two transformations can be applied sequentially:

$$H^{(2)} = (U_1 U_2) H^{(1)} (U_1 U_2)^\dagger - i \sum_{j=1,2} U_j \dot{U}_j^{-1}. \quad (\text{B4})$$

We expand the first term to second order in the small parameter β_j using the Hausdorff formula Eq. (3.8). For

the second term of Eq. (B4), we obtain to second order:

$$U_j \dot{U}_j^{-1} \approx \frac{1}{2} (\beta_j^* \dot{\beta}_j - \beta_j \dot{\beta}_j^*) \sigma_{z_j} + (\dot{\beta}_j \sigma_{-j} - \dot{\beta}_j^* \sigma_{+j}). \quad (\text{B5})$$

Choosing

$$\beta_j(t) = \frac{1}{2} \sum_{k=1,2} \frac{\Omega_{R_{jk}}}{\Delta_{a_{jk}}} e^{+i\omega_{d_k}t} \quad (\text{B6})$$

with $\Delta_{a_{jk}} = \omega_{a_j} - \omega_{d_k}$ and neglecting fast oscillating terms, we finally obtain

$$\begin{aligned} H^{(2)} \approx & \omega_r a^\dagger a + \sum_{j=1,2} \frac{\omega'_{a_j}}{2} \sigma_{z_j} + \varepsilon_3 (a^\dagger e^{-i\omega_3 t} + \text{h.c.}) \\ & - \sum_{j=1,2} g_j (\mu_j + s_j \sigma_{x_j}) (a^\dagger + a) \\ & - \sum_{j=1,2} g_j A_j (\beta_j^* \sigma_{+j} + \beta_j \sigma_{-j}) (a^\dagger + a) \\ & - \sum_{j=1,2} g_j B_j \sigma_{z_j} (a^\dagger + a), \end{aligned} \quad (\text{B7})$$

where the shifted qubit transition frequency is

$$\begin{aligned} \omega'_{a_j} = & \omega_{a_j} + \sum_{k=1,2} \frac{\Omega_{R_{jk}}^2}{2\Delta_{a_{jk}}} \\ & + \frac{\Omega_{R_{j1}} \Omega_{R_{j2}} (\Delta_{a_{j1}} + \Delta_{a_{j2}})}{2\Delta_{a_{j1}} \Delta_{a_{j2}}} \cos(\omega_{d_1} - \omega_{d_2}) t \end{aligned} \quad (\text{B8})$$

and

$$\begin{aligned} A_j = & 2c_j - s_j (\beta_j^* + \beta_j) \\ B_j = & 2c_j \left(|\beta_j|^2 - \frac{1}{2} \right) + s_j (\beta_j^* + \beta_j). \end{aligned} \quad (\text{B9})$$

In the presence of a single off-resonant drive, we recover Eq. (3.11).

Finally, the qubits are assumed to be strongly detuned from the resonator. We therefore adiabatically eliminate the direct Jaynes-Cummings qubit-resonator interaction. This is done using the dispersive transformation of Eq. (5.1). Since the rotating wave approximation was not performed on the qubit-resonator interaction, this choice of transformation will not cancel completely the interaction. Complete cancelation could be obtained by choosing a slightly different transformation. However, for the transitions of interest here, the remaining terms will be oscillating rapidly and will simply be dropped. Taking into account these terms would, again, only add a small frequency shift [51] that can safely be ignored here.

Applying the dispersive transformation Eq. (5.1), expanding to second order in the small parameter g_j / Δ'_j and neglecting fast oscillating terms, we obtain the main result of this appendix

$$\begin{aligned}
H^{(3)} \approx & \omega_r a^\dagger a + \sum_{j=1,2} \frac{\omega_{a_j}''}{2} \sigma_{z_j} + \varepsilon_3 (a^\dagger e^{-i\omega_{d_3}t} + a e^{+i\omega_{d_3}t}) - \sum_{j=1,2} \frac{\varepsilon_3}{2} \left(\frac{g_j s_j}{\Delta'_j} \right)^2 (a^\dagger e^{-i\omega_{d_3}t} + a e^{+i\omega_{d_3}t}) \sigma_{z_j} \\
& - \sum_{j=1,2} g_j B_j \sigma_{z_j} (a^\dagger + a) + s_1 s_2 \frac{g_1 g_2 (\Delta'_1 + \Delta'_2)}{2 \Delta'_1 \Delta'_2} (\sigma_{+1} \sigma_{-2} + \sigma_{-1} \sigma_{+2}) \\
& - \sum_{j,k=1,2} c_j g_j \frac{\Omega_{R_{jk}}}{\Delta_{a_{jk}}} (\sigma_{+j} e^{-i\omega_{d_k}t} + \sigma_{-j} e^{+i\omega_{d_k}t}) (a^\dagger + a) \\
& + \sum_{j,k,k'=1,2} s_j g_j \frac{\Omega_{R_{jk}}}{2 \Delta_{a_{jk}}} \frac{\Omega_{R_{jk'}}}{2 \Delta_{a_{jk'}}} \left\{ (e^{+i(\omega_{d_k} - \omega_{d_{k'}})t} + e^{-i(\omega_{d_k} + \omega_{d_{k'}})t}) \sigma_{+j} + (e^{-i(\omega_{d_k} - \omega_{d_{k'}})t} + e^{+i(\omega_{d_k} + \omega_{d_{k'}})t}) \sigma_{-j} \right\} (a^\dagger + a),
\end{aligned} \tag{B10}$$

where the shifted qubit transition frequency is

$$\omega_{a_j}'' = \omega_{a_j}' + 2s_j^2 \frac{g_j^2}{\Delta'_j} \left(a^\dagger a + \frac{1}{2} \right) \tag{B11}$$

and we have defined

$$\Delta'_j = \omega_{a_j}' - \omega_r. \tag{B12}$$

This effective Hamiltonian contains all the physics needed to realize each of the different gates that are studied in this paper. More particularly, the first term in the second line of (B10) can be used to generate a geometric two-qubit phase gate [25, 26] and is studied in more details in section VIII. The second term of the second line of equation (B10) is the flip-flop interaction due to virtual interaction with the resonator and is discussed in section V. We note that higher order flip-flop terms induced by the external drives have been dropped. Finally, as discussed in section VII B, the last two lines describe one and two photon blue and red sideband transitions.

APPENDIX C: RED AND BLUE SIDEBANDS USING FLICFORQ

Here we consider a single qubit coupled to the resonator and in the presence of a single drive of frequency ω_a and amplitude ε . For simplicity, we work at charge degeneracy and in the rotating wave-approximation:

$$\begin{aligned}
H = & \omega_r a^\dagger a + \frac{\omega_a}{2} \sigma_z - g(a^\dagger \sigma_- + \sigma_+ a) \\
& + \varepsilon(a^\dagger e^{-i\omega_a t} + a e^{i\omega_a t}).
\end{aligned} \tag{C1}$$

We again assume that the qubit is far detuned from the resonator frequency. However, we choose not to adiabatically eliminate the qubit-resonator interaction and look at a non-perturbative result for large drive amplitude. To find the effective qubit-resonator Hamiltonian in this case, we move to a frame where a non-vanishing interaction remains, but only when a resonance condition to be determined is satisfied.

We first move to a frame rotating at the qubit transition frequency ω_a for both the qubit and the resonator:

$$H^{(1)} = -\Delta a^\dagger a - g(a^\dagger \sigma_- + \sigma_+ a) + \varepsilon(a^\dagger + a), \tag{C2}$$

with $\Delta = \omega_a - \omega_r$. We then displace the resonator field using the displacement operator $D(\alpha)$ to obtain

$$H^{(2)} = -\Delta a^\dagger a - g(a^\dagger \sigma_- + \sigma_+ a) - \frac{\Omega_R}{2} \sigma_x. \tag{C3}$$

For convenience, we now change σ_x to $-\sigma_z$ using a rotation along the y axis of angle $-\pi/2$. After that rotation, the system looks like a qubit of frequency Ω_R coupled to a resonator of frequency Δ :

$$H^{(3)} = -\Delta a^\dagger a + \frac{\Omega_R}{2} \sigma_z + \frac{g}{2} (a^\dagger + a) \sigma_z + i \frac{g}{2} (a^\dagger - a) \sigma_y. \tag{C4}$$

Going to a frame rotating at both the new effective qubit and cavity frequencies, we obtain a single non-oscillating term when $\Delta = -\Omega_R$:

$$H_r^{(4)} \approx -\frac{g}{2} (a^\dagger \sigma_- + \sigma_+ a). \tag{C5}$$

and for $\Delta = \Omega_R$ we obtain:

$$H_b^{(4)} \approx \frac{g}{2} (a^\dagger \sigma_+ + \sigma_- a). \tag{C6}$$

These correspond, in the rotating frame, to red and blue sideband transitions at a rate $g/2$. The factor of $1/2$ is due to the fact that only one of the Rabi sidebands for the ground and excited states of the qubit are in resonance at $\Delta = \pm \Omega_R$. This type of qubit-cavity resonance was also discussed in Refs. [52] and [53].

APPENDIX D: FLICFORQ WITH TWO QUBITS

To obtain the effective Hamiltonian for the two-qubit FLICFORQ, we follow the results of appendix B and of Ref. [38]. The starting point is the Hamiltonian (B1)

taken in the rotating wave approximation and at charge degeneracy for both qubits ($s_j = 1, c_j = 0$). Moreover, we omit the measurement drive and consider only two coherent drives ($k = 1, 2$). To get maximal splitting of the Rabi sidebands, the frequency of these drive are chosen such that ω_{d_j} is close to ω_{a_j} .

To derive the effective Hamiltonian, we follow the same steps as in appendix B. The main difference is that in the second step, because of our choice of drive frequencies, we do not adiabatically eliminate both drives from both qubits. We adiabatically eliminate only the effect of ω_{d_1} on the second qubit and the effect of ω_{d_2} on the first qubit. The resulting effective Hamiltonian is

$$H \approx \omega_r a^\dagger a + \sum_{j=1,2} \frac{\omega_{a_j}''}{2} \sigma_{z_j} + \sum_{j=1,2} \frac{\Omega_{R_j}}{2} (\sigma_{+j} e^{-i\omega_{d_j} t} + \sigma_{-j} e^{+i\omega_{d_j} t}) + \frac{g_1 g_2 (\Delta'_1 + \Delta'_2)}{2\Delta'_1 \Delta'_2} (\sigma_{+1} \sigma_{-2} + \sigma_{-1} \sigma_{+2}), \quad (\text{D1})$$

where $\Delta'_j = \omega'_{a_j} - \omega_r$ and

$$\omega'_{a_{1(2)}} = \omega_{a_{1(2)}} + 2 \frac{\Omega_{R_{12(21)}}^2}{\Delta_{a_{12(21)}}}. \quad (\text{D2})$$

Assuming for simplicity that $\omega_{d_j} = \omega''_{a_j}$, we first go to a frame rotating at ω_{d_j} for qubit j . Following ref. [38], we then go to a frame rotating along the x axis and at a frequency $\Omega_{R_j}/2$ for qubit j . This yields

$$H \approx \omega_r a^\dagger a + \frac{g_1 g_2 (\Delta'_1 + \Delta'_2)}{8\Delta'_1 \Delta'_2} \times \{ [\sigma_{x_1} - i \sin(\Omega_{R_1} t) \sigma_{z_1} + i \cos(\Omega_{R_1} t) \sigma_{y_1}] \times [\sigma_{x_2} - i \sin(\Omega_{R_2} t) \sigma_{z_2} - i \cos(\Omega_{R_2} t) \sigma_{y_2}] e^{+i(\omega_{d_1} - \omega_{d_2})t} + \text{h.c.} \}. \quad (\text{D3})$$

We now look for terms that do not average to zero. These will correspond to resonance in the coupled driven system. There are several choices of resonances here and, as an example, we choose $\omega_{d_2} - \omega_{d_1} = \Omega_{R_1} + \Omega_{R_2}$. Using this condition, all terms but a single term are oscillating rapidly and average out to zero. The resulting effective Hamiltonian in the quadruply-rotating frame is

$$H_{\text{FF}} \approx \omega_r a^\dagger a + \frac{g_1 g_2 (\Delta'_1 + \Delta'_2)}{16\Delta'_1 \Delta'_2} (\sigma_{y_1} \sigma_{y_2} + \sigma_{z_1} \sigma_{z_2}). \quad (\text{D4})$$

Other choices of resonances lead to different symmetry for the effective Hamiltonian. These other possible coupling Hamiltonians will be discussed elsewhere.

APPENDIX E: SYMMETRY AND SELECTION RULES

At the charge degeneracy point, the Hamiltonian (2.3) is even in the number of creation and annihilation operators. As a result, $C \equiv a^\dagger a + \sigma_z/2$ commutes with the Hamiltonian and the total excitation number is a conserved quantity. On the other hand, away from charge degeneracy, in addition to the regular Jaynes-Cummings term, we get extra terms of the form $g(\mu + c\sigma_z)(a^\dagger + a)$ which are of odd parity in the number of creation and annihilation operators. Clearly, C is not a conserved quantity in this case.

These symmetry considerations will impose selection rules on the transitions that are possible. To see this more explicitly, we introduce the parity operator $P = e^{-i\pi a^\dagger a} \sigma_z$ which is the natural unitary extension of C [54, 55]. By writing the parity operator in the form $P = \sum_{n=0}^{\infty} (-1)^n |n\rangle \langle n| \sigma_z$, it is simple to verify that P anti-commutes with the drive Hamiltonian (3.1) in a frame rotating at the drive frequency. Labeling states as being of even (odd) parity if they are eigenstates of P with +1 (-1) eigenvalue, it is then clear that the drive $(a^\dagger + a)$ can only cause transitions between states of different parities.

To see which transitions are allowed at the sweet spot, we first give the parity of the eigenstates of the Jaynes-Cummings Hamiltonian:

$$P|g0\rangle = -|g0\rangle, \quad P|\overline{\pm, n}\rangle = (-1)^n |\overline{\pm, n}\rangle, \quad (\text{E1})$$

where [14]

$$|\overline{+, n}\rangle = \cos \theta_n |\downarrow, n\rangle + \sin \theta_n |\uparrow, n+1\rangle \quad (\text{E2})$$

$$|\overline{-, n}\rangle = -\sin \theta_n |\downarrow, n\rangle + \cos \theta_n |\uparrow, n+1\rangle \quad (\text{E3})$$

and

$$\theta_n = \frac{1}{2} \tan^{-1} \left(\frac{2g\sqrt{n+1}}{\Delta} \right). \quad (\text{E4})$$

The red sideband transition illustrated in Fig. 6a) corresponds to a transition between $|\overline{+, 0}\rangle$ and $|\overline{-, 0}\rangle$, it is therefore forbidden to first order. This is the result already obtained in Eq. (7.5). In the same way, the blue sideband corresponds to a transition between $|g0\rangle$ and $|\overline{-, 1}\rangle$. It is also forbidden at charge degeneracy. Single-photon Rabi flopping discussed in section III A connects $|g0\rangle$ and $|\overline{-, 0}\rangle$, and it is obviously allowed at charge degeneracy. In the case of two photon transitions, the drive Hamiltonian is effectively acting twice and the previous selection rules are therefore simply reversed. Finally, away from the charge degeneracy point, the Hamiltonian has no definite parity and these considerations do not apply. All sideband transitions are therefore allowed.

[1] M. H. Devoret, A. Wallraff, and J. M. Martinis (2004), cond-mat/0411174.

[2] G. Wendin and V. S. Shumeiko, *Superconducting quantum circuits, qubits and computing* (2005), cond-mat/0508729.

[3] A. Wallraff, D. I. Schuster, A. Blais, L. Frunzio, J. Majer, M. H. Devoret, S. M. Girvin, and R. J. Schoelkopf, Phys. Rev. Lett. **95**, 060501 (2005).

[4] I. Chiorescu, Y. Nakamura, C. Harmans, and J. Mooij, Science **299**, 1869 (2003).

[5] D. Vion, A. Aassime, A. Cottet, P. Joyez, H. Pothier, C. Urbina, D. Esteve, and M. Devoret, Science **296**, 886 (2002).

[6] J. Martinis, S. Nam, J. Aumentado, and C. Urbina, Phys. Rev. Lett. **89**, 117901 (2002).

[7] Y. Nakamura, Y. Pashkin, and J. Tsai, Nature (London) **398**, 786 (1999).

[8] R. McDermott, R. W. Simmonds, M. Steffen, K. B. Cooper, K. Cicak, K. D. Osborn, S. Oh, D. P. Pappas, and J. M. Martinis, Science **307**, 1299 (2005).

[9] J. B. Majer, F. G. Paauw, A. C. J. ter Haar, C. J. P. M. Harmans, and J. E. Mooij, Phys. Rev. Lett. **94**, 090501 (2005).

[10] T. Yamamoto, Y. A. Pashkin, O. Astafiev, Y. Nakamura, and J. Tsai, Nature **425**, 941 (2003).

[11] A. J. Berkley, H. Xu, R. C. Ramos, M. A. Gubrud, F. W. Strauch, P. R. Johnson, J. R. Anderson, A. J. Dragt, C. J. Lobb, and F. C. Wellstood, Science **300**, 1548 (2003).

[12] Y. A. Pashkin, T. Yamamoto, O. Astafiev, Y. Nakamura, D. Averin, and J. Tsai, Nature **421**, 823 (2003).

[13] M. Steffen, M. Ansmann, R. C. Bialczak, N. Katz, E. Lucero, R. McDermott, M. Neeley, E. M. Weig, A. N. Cleland, and J. M. Martinis, Science **313**, 1423 (2006).

[14] A. Blais, R.-S. Huang, A. Wallraff, S. M. Girvin, and R. J. Schoelkopf, Phys. Rev. A **69**, 062320 (2004).

[15] A. Wallraff, D. I. Schuster, A. Blais, L. Frunzio, R.-S. Huang, J. Majer, S. Kumar, S. M. Girvin, and R. J. Schoelkopf, Nature **431**, 162 (2004).

[16] D. I. Schuster, A. Wallraff, A. Blais, L. Frunzio, R.-S. Huang, J. Majer, S. M. Girvin, and R. J. Schoelkopf, Phys. Rev. Lett. **94**, 123602 (2005).

[17] J. Gambetta, A. Blais, D. I. Schuster, A. Wallraff, L. Frunzio, J. Majer, M. H. Devoret, S. M. Girvin, and R. J. Schoelkopf, Physical Review A (Atomic, Molecular, and Optical Physics) **74**, 042318 (2006).

[18] D. I. Schuster, A. A. Houck, J. A. Schreier, A. Wallraff, J. M. Gambetta, A. Blais, L. Frunzio, B. Johnson, M. H. Devoret, S. M. Girvin, et al. (2006), cond-mat/0608693.

[19] A. Blais, Phys. Rev. A **64**, 022312 (2001).

[20] D. Gottesman, J. Mod. Opt. **47**, 333 (2000).

[21] D. Aharonov and M. Ben-Or, in *Proceedings of the 37th Annual Symposium on Foundations of Computer Science* (IEEE Comput. Soc. Press, 1996), p. 46.

[22] J. F. Poyatos, J. I. Cirac, and P. Zoller, Phys. Rev. Lett. **78**, 390 (1997).

[23] R. W. Simmonds, K. M. Lang, D. A. Hite, S. Nam, D. P. Pappas, and J. M. Martinis, Physical Review Letters **93**, 077003 (2004).

[24] O. Gywat, F. Meier, D. Loss, and D. D. Awschalom, Physical Review B (Condensed Matter and Materials Physics) **73**, 125336 (2006).

[25] J. J. Garcia-Ripoll, P. Zoller, and J. I. Cirac, Phys. Rev. Lett. **91**, 157901 (2003).

[26] J. J. Garcia-Ripoll, P. Zoller, and J. I. Cirac, Phys. Rev. A **71**, 062309 (2005).

[27] V. Bouchiat, D. Vion, P. Joyez, D. Esteve, and M. Devoret, Physica Scripta **T76**, 165 (1998).

[28] Y. Makhlin, G. Schön, and A. Shnirman, Rev. Mod. Phys. **73**, 357 (2001).

[29] L. Frunzio, A. Wallraff, D. I. Schuster, J. Majer, and R. J. Schoelkopf, in *IEEE Transactions on Applied Superconductivity Proceedings of Applied Superconductivity Conference, Jacksonville, FL* (2004), vol. 15, p. 860.

[30] D. Walls and G. Milburn, *Quantum optics* (Springer-Verlag, Berlin, 1994).

[31] P. K. Day, H. G. LeDuc, B. A. Mazin, A. Vayonakis, and J. Zmuidzinas, Nature **425**, 817 (2003).

[32] E. Collin, G. Ithier, A. Aassime, P. Joyez, D. Vion, and D. Esteve, Phys. Rev. Lett. **93**, 157005 (2004).

[33] C. Slichter, *Principles of Magnetic Resonance* (Springer-Verlag, 1990), 3rd ed.

[34] K. M. Fonseca-Romero, S. Kohler, and P. Hanggi, Phys. Rev. Lett. **95**, 140502 (2005).

[35] J. Cirac and P. Zoller, Phys. Rev. Lett. **74**, 4091 (1995).

[36] A. M. Childs and I. L. Chuang, Phys. Rev. A **63**, 012306 (2000).

[37] M. Wallquist, V. Shumeiko, and G. Wendin (2006), cond-mat/0608209.

[38] C. Rigetti, A. Blais, and M. Devoret, Phys. Rev. Lett. **94**, 240502 (2005).

[39] A. Sørensen and K. Mølmer, Phys. Rev. Lett. **82**, 1971 (1999).

[40] A. Imamoglu, D. D. Awschalom, G. Burkard, D. P. DiVincenzo, D. Loss, M. Sherwin, and A. Small, Phys. Rev. Lett. **83**, 4204 (1999).

[41] S.-B. Zheng and G.-C. Guo, Phys. Rev. Lett. **85**, 2392 (2000).

[42] A. Barenco, C. Bennett, R. Cleve, D. DiVincenzo, N. Margolus, S. P. T. Sleator, J. Smolin, and H. Weinfurter, Phys. Rev. A **52**, 3457 (1995).

[43] G. Ithier, E. Collin, P. Joyez, P. J. Meeson, D. Vion, D. Esteve, F. Chiarello, A. Shnirman, Y. Makhlin, J. Schriefl, et al., Phys. Rev. B **72**, 134519 (2005).

[44] R. Ruskov, A. N. Korotkov, and A. Mizel, Physical Review Letters **96**, 200404 (2006).

[45] H. Haffner, W. Hansel, C. F. Roos, J. Benhelm, D. Chekalakar, M. Chwalla, T. Korber, U. D. Rapol, M. Riebe, P. O. Schmidt, et al., Nature **438**, 643 (2005).

[46] D. Leibfried, E. Knill, S. Seidelin, J. Britton, R. B. Blakestad, J. Chiaverini, D. B. Hume, W. M. Itano, J. D. Jost, C. Langer, et al., Nature **438**, 639 (2005).

[47] J. Q. You and F. Nori, Phys. Rev. B **68**, 064509 (2003).

[48] C.-P. Yang and S. Han, Physical Review A (Atomic, Molecular, and Optical Physics) **73**, 032317 (2006).

[49] E. Aarts and J. Korst, *Simulated Annealing and Boltzmann Machines* (Wiley, New York, 1989).

[50] A. Blais, A. Maassen van den Brink, and A. Zagoskin, Phys. Rev. Lett. **90**, 127901 (2003).

[51] F. Bloch and A. Siegert, Phys. Rev. **57**, 522 (1940).

[52] D. Jonathan, M. B. Plenio, and P. L. Knight, Phys. Rev. A **62**, 042307 (2000).

[53] E. Solano, G. S. Agarwal, and H. Walther, Phys. Rev.

Lett. **90**, 027903 (2003).

[54] C. F. Lo, K. L. Liu, K. M. Ng, and P. H. Yuen, Quantum Semiclass. Opt. **10**, L63 (1998).

[55] M. A. Talab, S. Guérin, and H. R. Jauslin, J. Math. Phys. **46**, 042311 (2005).

[56] Here we use $-g$ instead of $+g$. We have dropped this unimportant minus sign in Ref. [14].

[57] Note the change of convention for the operators σ_+ and σ_- from Ref. [36]. Here, we explicitly work in the $\{|e\rangle, |g\rangle\}$ basis and σ_+ takes $|g\rangle$ to $|e\rangle$ as usual.

[58] It is possible that the present approach could work beyond n_{crit} with proper pulse shaping and timing, but investigating this regime requires extensive numerical calculations that are beyond the scope of this paper.